



CO and Dust Properties in the TW Hya Disk from High-resolution ALMA Observations

Jane Huang¹, Sean M. Andrews¹, L. Ilseadore Cleeves^{1,10}, Karin I. Öberg¹, David J. Wilner¹, Xuening Bai^{1,2,3}, Til Birnstiel⁴, John Carpenter⁵, A. Meredith Hughes⁶, Andrea Isella⁷, Laura M. Pérez⁸, Luca Ricci⁷, and Zhaohuan Zhu⁹

¹Harvard-Smithsonian Center for Astrophysics, 60 Garden Street, Cambridge, MA 02138, USA; jane.huang@cfa.harvard.edu

²Institute for Advanced Study, Tsinghua University, Beijing 100084, People's Republic of China

³Tsinghua Center for Astrophysics, Tsinghua University, Beijing 100084, People's Republic of China

⁴University Observatory, Faculty of Physics, Ludwig-Maximilians-Universität München, Scheinerstr. 1, D-81679 Munich, Germany

⁵Joint ALMA Observatory, Alonso de Cordova 3107 Vitacura—Santiago de Chile, Chile

⁶Van Vleck Observatory, Astronomy Department, Wesleyan University, 96 Foss Hill Drive, Middletown, CT 06459, USA

⁷Department of Physics and Astronomy, Rice University, 6100 Main Street, Houston, TX 77005, USA

⁸Departamento de Astronomía, Universidad de Chile, Casilla 36-D, Santiago, Chile

⁹Department of Physics and Astronomy, University of Nevada, Las Vegas, 4505 South Maryland Parkway, Las Vegas, NV 89154, USA

Received 2017 October 30; revised 2017 December 8; accepted 2017 December 12; published 2018 January 15

Abstract

We analyze high angular resolution ALMA observations of the TW Hya disk to place constraints on the CO and dust properties. We present new, sensitive observations of the $^{12}\text{CO } J = 3 - 2$ line at a spatial resolution of 8 au ($0''.14$). The CO emission exhibits a bright inner core, a shoulder at $r \approx 70$ au, and a prominent break in slope at $r \approx 90$ au. Radiative transfer modeling is used to demonstrate that the emission morphology can be reasonably reproduced with a ^{12}CO column density profile featuring a steep decrease at $r \approx 15$ au and a secondary bump peaking at $r \approx 70$ au. Similar features have been identified in observations of rarer CO isotopologues, which trace heights closer to the midplane. Substructure in the underlying gas distribution or radially varying CO depletion that affects much of the disk's vertical extent may explain the shared emission features of the main CO isotopologues. We also combine archival 1.3 mm and $870 \mu\text{m}$ continuum observations to produce a spectral index map at a spatial resolution of 2 au. The spectral index rises sharply at the continuum emission gaps at radii of 25, 41, and 47 au. This behavior suggests that the grains within the gaps are no larger than a few millimeters. Outside the continuum gaps, the low spectral index values of $\alpha \approx 2$ indicate either that grains up to centimeter size are present or that the bright continuum rings are marginally optically thick at millimeter wavelengths.

Key words: astrochemistry – ISM: molecules – protoplanetary disks – stars: individual (TW Hydrae)

1. Introduction

Tracing the distribution of dust and volatiles in protoplanetary disks is key for guiding models of planet formation. Disk observations may be useful for constraining the formation locations of planets (e.g., Öberg et al. 2011; Zhu et al. 2014; Dong et al. 2015), the mechanisms by which the dust and gas distributions in disks evolve to form planets and planetesimals (e.g., Pérez et al. 2012; Birnstiel et al. 2015; van der Marel et al. 2015), and the abundances of volatiles that will eventually be incorporated into planetary atmospheres (e.g., Cridland et al. 2016; Eistrup et al. 2016; Öberg & Bergin 2016).

Millimeter/submillimeter interferometry plays a fundamental role in characterizing disk structures owing to the high spatial resolution and sensitivity that can be achieved for observations of both dust and molecular emission. Observations of the millimeter continuum, which is dominated by thermal emission from millimeter-sized grains, can test models of grain growth and transport (e.g., Birnstiel et al. 2010; Ricci et al. 2010; Guilloteau et al. 2011; Andrews et al. 2012). CO is often targeted simultaneously with continuum observations; as an abundant and easily observable molecule, CO is used to infer fundamental properties such as gas masses and temperatures (e.g., Dartois et al. 2003; Rosenfeld et al. 2013; Williams & Best 2014). In addition, since CO is the primary gas-phase carbon reservoir in disks, characterizing its distribution is also pertinent to predicting the abundances and distribution of many

other species that are major components of the gas and ice incorporated into planets and planetesimals (e.g., Aikawa & Herbst 1999; Reboussin et al. 2015).

Due to its proximity, relative isolation, bright emission, and nearly face-on orientation, the TW Hya disk (J2000 R.A. $11^{\text{h}}01^{\text{m}}51^{\text{s}}.905$, decl. $-34^{\circ}42'17''.03$) has long served as a template for protoplanetary disks, spurring the development of techniques, models, and lines of inquiry that have since been extended to other sources (e.g., Calvet et al. 2002; van Dishoeck et al. 2003; Qi et al. 2004, 2013; Bergin et al. 2013). TW Hya is a 10 Myr old K6 star in the TW Hydrae association lying 59.5 pc away from Earth (e.g., Kastner et al. 1997; Webb et al. 1999; Torres et al. 2006; Weinberger et al. 2013; Gaia Collaboration et al. 2016). Intriguingly, recent observations have revealed concentric rings and gaps in millimeter/submillimeter continuum emission tracing the distribution of large dust grains near the midplane (Andrews et al. 2016; Tsukagoshi et al. 2016), scattered-light observations tracing the distribution of small dust grains in the upper layers of the disk (e.g., Debes et al. 2013; Akiyama et al. 2015; Rapson et al. 2015; van Boekel et al. 2017), and molecular line emission (e.g., Nomura et al. 2016; Schwarz et al. 2016; Teague et al. 2017). The origins of these features and their relationships to one another are not yet definitively established. Embedded planets, molecular snowlines, structured magnetohydrodynamic turbulence, and photoevaporation are often invoked as hypotheses to explain the types of features observed in the TW Hya disk (see aforementioned references and, e.g.,

¹⁰ Hubble Fellow.

Table 1
ALMA Observation Summary

Program	P.I.	References	Date	Freq. Range (GHz)	Antennas	Baselines (m)	On-source Time (minutes)	Notes
(1)	(2)	(3)	(4)	(5)	(6)	(7)	(8)	(9)
Band 6 Observations								
2013.1.00114.S	K. I. Öberg	1, 2	2014 Jul 19	225.650–242.015	32	34–650	43	Continuum
2013.1.00387.S	S. Guilloteau	3	2015 May 13	226.617–244.940	36	21–558	46	Continuum
2015.A.00005.S	T. Tsukagoshi	2	2015 Dec 1	223.007–242.992	35	17–10804	39	Continuum
Band 7 Observations								
2012.1.00422.S	E. A. Bergin	4	2015 May 14	330.304–330.539 ^a	37	21–558	20	¹³ CO
2013.1.00196.S	P. Hily-Blant	...	2014 Dec 24	330.595–330.653 ^a	40	15–349	38	¹³ CO
			2015 Apr 04	330.540–330.599 ^a	38	15–328	75	
2013.1.00198.S	E. A. Bergin	5, 6	2014 Dec 31	337.353–352.011	34	15–349	15	Continuum
			2015 Jun 15	337.299–352.192	36	21–784	30	
2013.1.01397.S	D. Ishimoto	7	2015 May 19	329.236–342.904	35	21–539	27	¹³ CO + Continuum
			2015 May 20	329.236–342.904	39	21–539	27	
2015.1.00686.S	S. M. Andrews	8	2015 Nov 23	345.492–358.057	36	23–8259	41	¹² CO+ Continuum
			2015 Nov 30	345.494–358.059	31	27–10804	43	
			2015 Dec 1	345.494–358.059	34	17–10804	43	
2016.1.00629.S	L. I. Cleeves	...	2016 Dec 30	345.780–345.839 ^a	45	15–460	33	¹² CO
			2016 Dec 30	345.780–345.839 ^a	45	15–460	18	
			2017 Jul 4	345.726–345.785 ^a	44	21–2600	44	
			2017 Jul 9	345.726–345.785 ^a	42	17–2600	44	
			2017 Jul 14	345.727–345.787 ^a	42	19–1500	44	
			2017 Jul 20	345.728–345.787 ^a	42	17–3700	44	
			2017 Jul 21	345.728–345.787 ^a	42	17–3700	44	

Note.

^a These observations also included additional spectral windows at other frequencies. The line-free channels were not incorporated into the main continuum analysis in this work owing to the relatively small continuum bandwidth available.

References. (1) Walsh et al. 2016; (2) Tsukagoshi et al. 2016; (3) Teague et al. 2016; (4) Schwarz et al. 2016; (5) Zhang et al. 2016; (6) Bergin et al. 2016; (7) Nomura et al. 2016; (8) Andrews et al. 2016.

Flock et al. 2015; Zhang et al. 2015; Dong et al. 2017; Ercolano et al. 2017).

To place additional constraints on the dust and CO distributions in the TW Hya disk, we analyze new high angular resolution ALMA observations of the ¹²CO $J = 3 - 2$ transition, as well as a spectral index map produced from archival 1.3 mm and 870 μ m continuum observations. The data reduction is described in Section 2. The observed line emission and continuum emission are described in Section 3, and radiative transfer modeling of the ¹²CO data is presented in Section 4. We provide a discussion in Section 5 and a summary in Section 6.

2. Observations and Data Reduction

2.1. Continuum Reduction

We reprocessed and combined archival 1.3 mm (Band 6) and 870 μ m (Band 7) continuum data from six ALMA programs. The raw data from programs 2013.1.00114.S, 2013.1.00198.S, and 2015.1.00686.S were calibrated by National Radio Astronomical Observatory (NRAO) staff, and the raw data from programs 2013.1.00387.S, 2015.A.00005.S, and 2013.1.01397.S were downloaded from the ALMA archive and calibrated in CASA (McMullin et al. 2007) using the accompanying reduction scripts. Table 1 summarizes the observation setups. Bright quasars were used for bandpass and phase calibration, and either a solar system object (using the Butler-JPL-Horizons 2012 model) or a bright

quasar was used for amplitude calibration. Table 3 (in Appendix A) lists calibrator details.

Additional calibration and imaging were performed with CASA 4.5.3. After flagging channels displaying strong line emission and data with anomalous amplitudes or phases, the line-free channels were spectrally averaged to form continuum visibility data sets. Data from the four programs observed with compact antenna configurations (2013.1.00114.S, 2013.1.00198.S, 2013.1.00387.S, and 2013.1.01397.S) were first individually imaged and phase self-calibrated. The continuum fluxes from the self-calibrated images were within 5% of one another within each band (measured within a 2.5 diameter region in the images to be ≈ 0.58 and ≈ 1.4 Jy for Bands 6 and 7, respectively), which is compatible with the estimated 10% systematic flux calibration uncertainty of ALMA in these bands. Since the high-resolution data sets (2015.1.00686.S and 2015.A.00005.S) only had a few baselines at uv distances below 200 k λ , the amplitudes of these visibilities were compared directly with those from the short-baseline data sets to check for consistency at corresponding uv distances. Because of the relatively large proper motion of TW Hya, the `fixvis` and `fixplanets` tasks in CASA were used to shift the data sets to a common phase center.

A high-resolution 1.3 mm continuum image was produced by combining the data from the three Band 6 programs and applying the multiscale multifrequency synthesis algorithm (Cornwell 2008), as implemented in the `clean` task. Briggs

weighting (robust = 0.5) and scales of $0''$, $0''.06$, $0''.15$, $0''.3$, and $0''.6$ were used. This generated a source model used to phase self-calibrate the data together. A similar self-calibration and imaging procedure was applied to the Band 7 data. The self-calibrated $870\ \mu\text{m}$ and $1.3\ \text{mm}$ continuum images were used to check for consistency with the images published in Andrews et al. (2016) and Tsukagoshi et al. (2016), which used the same long-baseline data and some of the same short-baseline data. The two continuum images and the deprojected, azimuthally averaged radial brightness temperature profiles are shown in Appendix B.

The self-calibrated $870\ \mu\text{m}$ and $1.3\ \text{mm}$ continuum data sets were then imaged together with the `clean` task's implementation of multiterm multifrequency synthesis (Rau & Cornwell 2011) with `nterms` = 2 and a Briggs robust parameter of 0. In brief, the imaging algorithm uses a first-order Taylor expansion to model the source intensity as a function of frequency, i.e.,

$$I_\nu = I_{\nu_0} \left(\frac{\nu}{\nu_0} \right)^\alpha \approx I_{\nu_0} \left(1 + \alpha \left(\frac{\nu - \nu_0}{\nu_0} \right) \right). \quad (1)$$

This procedure takes advantage of the additional uv coverage offered by wide-band imaging to produce a higher-fidelity continuum image compared to imaging the Band 6 or Band 7 data individually. In addition, simultaneously fitting for the spectral index α during the deconvolution process also reduces the influence of imaging artifacts that would arise from computing the spectral index from the Band 6 and 7 images individually. The combined continuum image is at a frequency of 290 GHz. The synthesized beam is $37 \times 26\ \text{mas}$ ($2.2 \times 1.5\ \text{au}$), with a position angle of $73^\circ.7$. The rms measured in a signal-free portion of the image is $20\ \mu\text{Jy beam}^{-1}$. The spectral index is computed only for pixels where the intensity image exceeds $0.1\ \text{mJy beam}^{-1}$ ($5 \times$ the rms noise).

2.2. $^{12}\text{CO } J = 3 - 2$ Data Reduction

The $^{12}\text{CO } J = 3 - 2$ transition in the TW Hya disk was observed with extended array configurations at channel widths of 244 kHz as part of ALMA program 2015.1.00686.S and with more compact configurations at channel widths of 61 kHz as part of ALMA program 2016.1.00629.S. The raw data for both programs were calibrated by NRAO staff. Details of the observation setups are listed in Table 1.

The phase self-calibration solutions used for the high-resolution $870\ \mu\text{m}$ continuum imaging were applied to the ^{12}CO observations from 2015.1.00686.S. The ^{12}CO observations from 2016.1.00629.S were phase self-calibrated using a continuum model estimated from the line-free channels in the same spectral window. The continuum was then subtracted from the line emission in the visibility plane using the `uvcontsub` task. Because the two programs were observed with different spectral resolutions, the `mstransform` task in CASA 5.0 was used to regrid and average the visibilities into channels $0.25\ \text{km s}^{-1}$ (288 kHz) wide. The ^{12}CO data sets were then imaged together with the multiscale CLEAN algorithm (as implemented in the `tclean` task in CASA 5.0) using scales of $0''$, $0''.2$, $0''.4$, $0''.8$, $1''.6$, and $3''.2$ and Briggs weighting (robust = 1.0).¹¹ The CLEAN mask was tailored to the emission in individual channels.

The resulting image has a synthesized beam with an FWHM of $139 \times 131\ \text{mas}$ ($8.3 \times 7.8\ \text{au}$) at a position angle of $-74^\circ.9$. The rms measured in nearby signal-free channels is $\approx 1.7\ \text{mJy beam}^{-1}$. A primary beam correction was applied to the image cube with the `impbcor` task. An integrated intensity map was produced by summing emission above the 3σ level in the velocity range from -1.91 to $7.59\ \text{km s}^{-1}$. This velocity range was chosen based on where the emission in the line wings exceeded the 3σ level, but the map is robust to choice of integration limits—truncating or extending the integration range by a few channels changed the integrated flux by less than 0.1%.

3. Observational Results

3.1. The Spectral Index between 1.3 mm and $870\ \mu\text{m}$

The 290 GHz (Band 6 + Band 7) continuum image, spectral index (α) map, and deprojected and azimuthally averaged radial profiles are shown in Figure 1. The adopted position angle and inclination are 152° and 5° , respectively, based on comparisons between spectral line models and data (see Section 4). These values are consistent within uncertainties with the orientation derived by Andrews et al. (2016) from the $870\ \mu\text{m}$ continuum. The inclination is slightly smaller than the commonly used value of 7° from Qi et al. (2004), but Qi et al. also use a lower stellar mass value, which is degenerate with inclination. We favor the higher stellar mass value of $0.88 M_\odot$ derived in Andrews et al. (2012) based on spectral energy distribution (SED) modeling. Given the low inclination of the TW Hya disk, the deprojected profiles are insensitive to inclination choices within a few degrees of one another.

The continuum emission appears to be azimuthally symmetric and shows prominent gaps at radii of 1, 25, 41, and 47 au, which is consistent with the Band 6 and Band 7 images published in Tsukagoshi et al. (2016) and Andrews et al. (2016). These and all subsequent measurements quoted from the literature are adjusted for the new *Gaia* distance of 59.5 pc (Gaia Collaboration et al. 2016).

The spectral index profile is mostly flat at radii coinciding with the bright continuum emission rings; α values range from 1.7 to 2.2, taking the scatter into account. The spectral index drops sharply to values close to 1 interior to a radius of 2 au, which is an unphysical consequence of the innermost gap only being partly resolved in Band 6. The spectral index profile also has local maxima with α peaking at ~ 2.6 – 2.7 near the locations of the continuum emission gaps at 25, 41, and 47 au. Tsukagoshi et al. (2016) measured the spectral index of TW Hya at 190 GHz and also reported a steep increase in α at 25 au, coincident with the most prominent gap in continuum emission. They tentatively suggested enhancements in α at the 41 and 47 au continuum gaps. Our 290 GHz spectral index map, which has an angular resolution about a factor of two higher than the map from Tsukagoshi et al. (2016), now confirms the presence of the latter two peaks.

While the spectral index radial profiles around 290 and 190 GHz have similar values in the inner 15 au of the disk, the α value around 290 GHz is consistently lower than that measured for 190 GHz at a given radius in the outer disk. This behavior is expected based on the dust optical depth increasing with frequency. A more striking difference between the

¹¹ A newer version of CASA was adopted for the line imaging as a result of a bug in the visibility interpolation of spectral line data in previous versions. See <https://casa.nrao.edu/casadocs/casa-5.0.0/introduction/release-notes-50>.

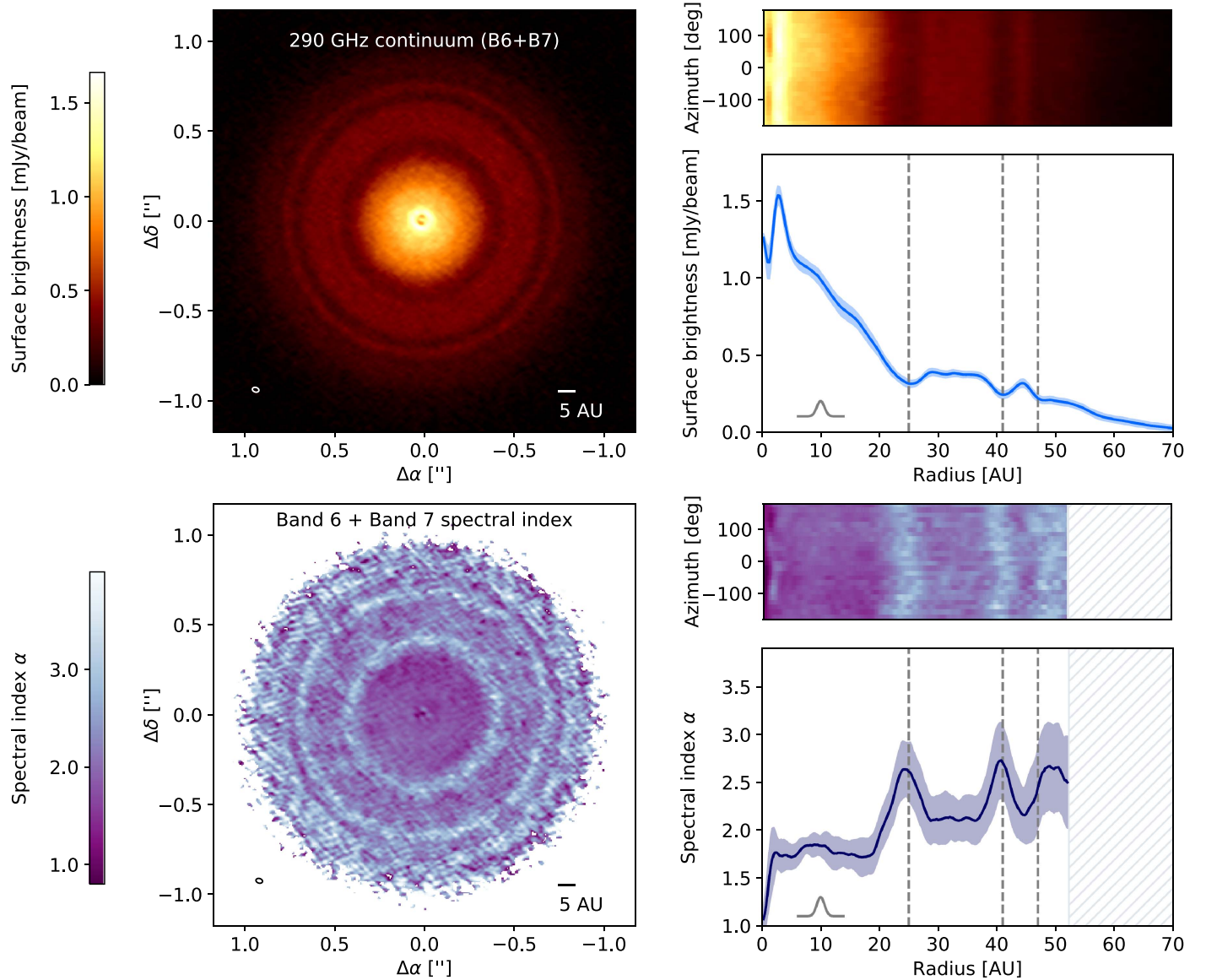


Figure 1. Top left: 290 GHz continuum image of the TW Hya disk generated from combining Band 6 and Band 7 data. The synthesized beam is shown in the lower left corner. Top right: 290 GHz continuum emission deprojected and replotted as a function of radius and azimuth, with the deprojected, azimuthally averaged radial surface brightness profile shown underneath. The light-blue ribbon shows the 1σ scatter of each radial bin. Gray dashed lines mark the location of the continuum gaps at 25, 41, and 47 au. The Gaussian profile shows the FWHM of the minor axis of the synthesized beam. Bottom left: spectral index map calculated from Band 6 and Band 7 data. Bottom right: spectral index map deprojected and replotted as a function of radius and azimuth, with its deprojected, azimuthally averaged radial profile shown underneath. The light-purple ribbon shows the 1σ scatter in each radial bin. Values are only shown out to a radius of 55 au because a substantial fraction of pixels in the continuum image past this radius fall below the signal-to-noise threshold of 5σ .

290 GHz spectral index radial profile presented in this work and that at 190 GHz presented in Tsukagoshi et al. (2016) is that the former displays more abrupt changes in α with radius, likely because the 290 GHz map is better resolved. We note that the relative shape of the α radial profile at a given frequency can be determined more robustly than the absolute value of α , since the systematic flux calibration uncertainty in each band contributes a constant offset to the entire profile. A $\sim 10\%$ flux uncertainty in each band would correspond to an uncertainty in the overall offset of $\Delta\alpha \sim 0.4$, but the uncertainty in the relative differences in α is governed by the scatter shown in Figure 1.

3.2. $^{12}\text{CO } J = 3 - 2$ Observations

3.2.1. $^{12}\text{CO } J = 3 - 2$ Emission Morphology

The ^{12}CO channel maps are shown in Figure 2. ^{12}CO emission exceeding the 3σ level extends to a radius of $\approx 3''6$ (215 au), which is consistent with Submillimeter Array observations reported in Andrews et al. (2012). The CO emission stretches well beyond the submillimeter continuum emission. The channel maps show three key features (see also annotations in Figure 3):

1. a bright core of emission extending out to a radius of ≈ 25 au;

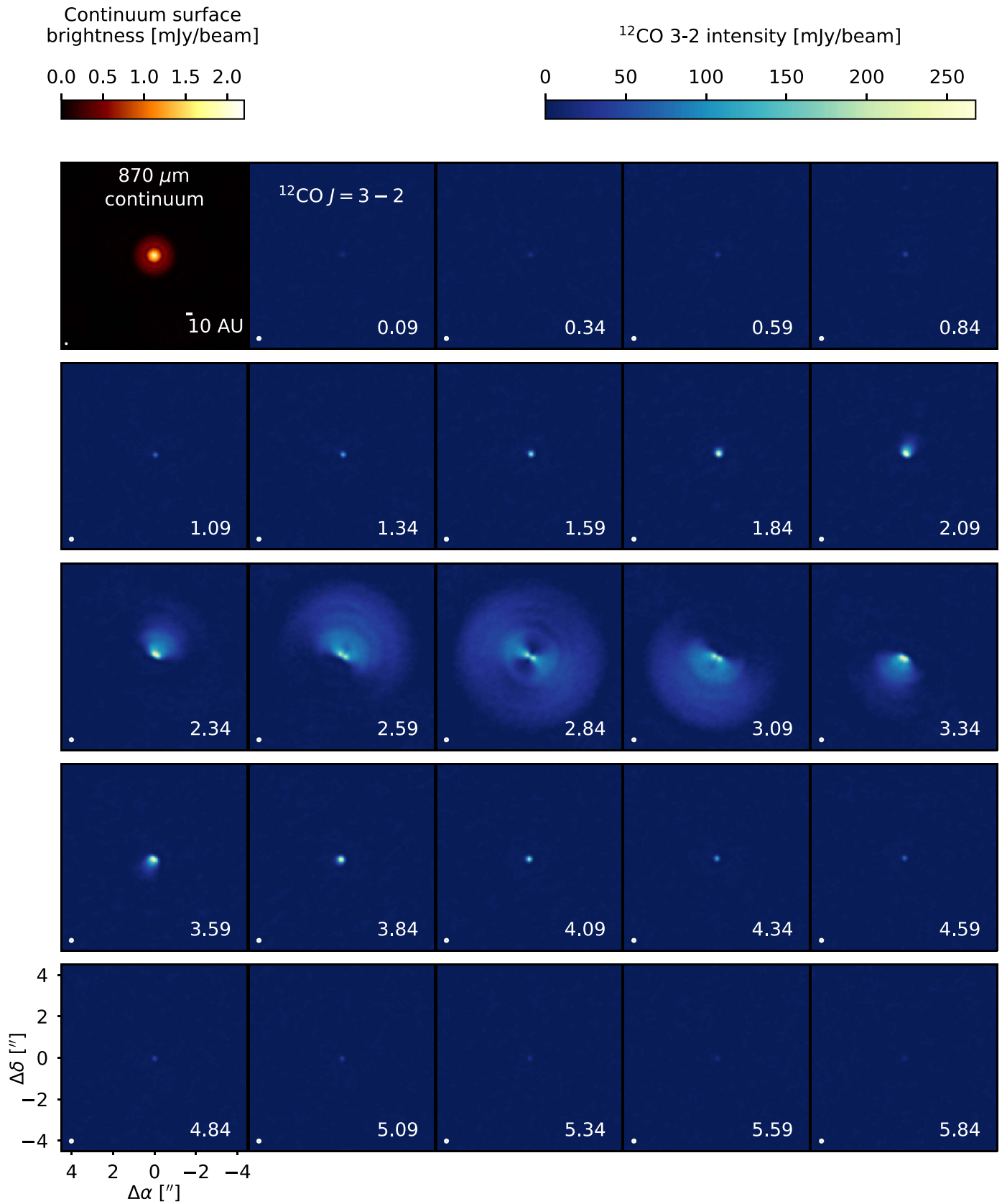


Figure 2. Channel maps of the $^{12}\text{CO } J = 3 - 2$ transition, along with the $870 \mu\text{m}$ continuum emission in the upper leftmost panel shown on the same spatial scale. Synthesized beams are drawn in the lower left corner of each panel. The LSR velocity (km s^{-1}) is shown in the lower right corner for each ^{12}CO channel.

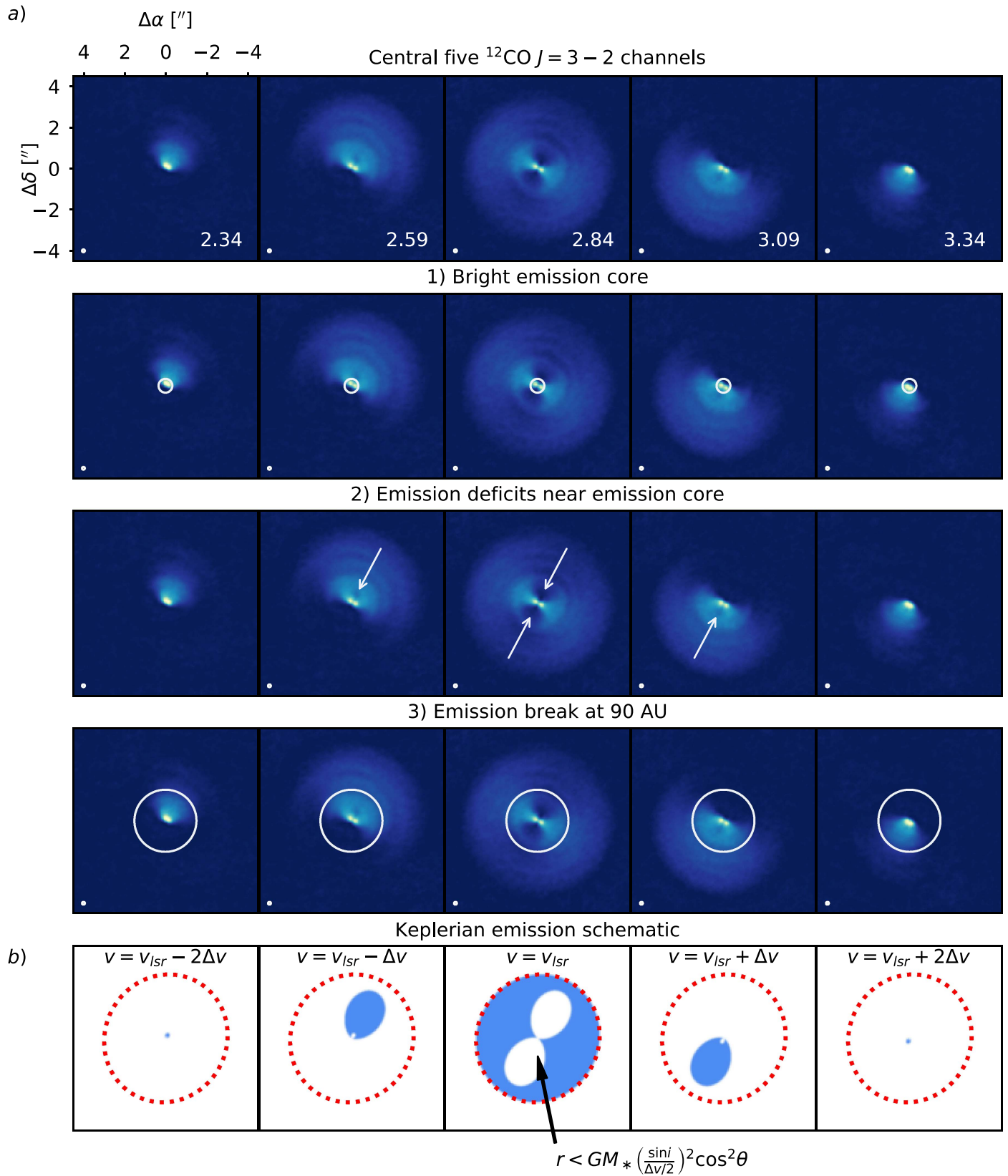


Figure 3. (a) Annotated maps of the central five channels of $^{12}\text{CO } J = 3 - 2$ to highlight the key emission features (see Figure 2 for context). (b) Schematic of the line emission morphology of a Keplerian disk (neglecting thermal and turbulent line broadening and beam smearing). The velocity is listed at the top of each panel. The dotted red ellipse marks the boundary of the projected disk. In the central panel at the systemic velocity, the region of the disk that contributes no emission is marked.

2. emission deficits along the disk major axis and adjacent to the bright emission core in the three central channels at 2.59, 2.84, and 3.09 km s⁻¹; and
3. a break in emission at a radius of ≈90 au.

An additional faint dark arc is visible in several channels at a radius of ∼125 au, but it is not clear whether this is simply an imaging artifact (see Section 4.2).

The emission deficits in the central channels are partly due to the disk inclination (see Guilloteau et al. 2006; Rosenfeld et al. 2013, for a more detailed discussion). For a geometrically thin disk undergoing Keplerian rotation and being viewed at an inclination angle of i , the projected velocity at a point (r, θ) in the disk is

$$v_{\text{proj}}(r, \theta) = v_{\text{LSR}} + \sqrt{\frac{GM_*}{r}} \sin i \cos \theta. \quad (2)$$

Here r and θ are in cylindrical coordinates in the frame of the disk, with $\theta = 0$ located along the major axis of the disk as seen by an observer. Assuming infinite spatial and spectral resolution and neglecting other line-broadening effects, only the region of the disk satisfying

$$r = GM_* \left(\frac{\sin i}{v_{\text{proj}} - v_{\text{LSR}}} \right)^2 \cos^2 \theta \quad (3)$$

contributes to emission observed in a channel at v_{proj} .

At the systemic velocity of 2.84 km s⁻¹, Equation (3) collapses into a line along the minor axis of the projected disk, which is aligned with the bright “hourglass” emission core observed in the TW Hya channel maps. Every channel in reality has nonzero spectral resolution, so it incorporates emission from $v_{\text{proj}} \pm \frac{\Delta v}{2}$, where Δv is the channel width (still neglecting other line-broadening effects). Then, the channel at the systemic velocity includes emission from disk regions satisfying

$$r \geq GM_* \left(\frac{\sin i}{\frac{\Delta v}{2}} \right)^2 \cos^2 \theta. \quad (4)$$

This geometry creates emission deficits along the major axis of the disk, near the disk center (see Figure 3(b)), but in Section 4 we will use radiative transfer models to argue that viewing angle does not wholly account for these features in the TW Hya disk.

The ¹²CO integrated intensity map and corresponding deprojected and azimuthally averaged radial profile are shown in Figure 4. The integrated intensity profile is centrally peaked but rapidly decreases out to a radius of ≈30 au, where the slope of the intensity profile abruptly flattens. The profile exhibits a shoulder at a radius of 70 au, decreases more rapidly out to a radius of 90 au, and then flattens out and tapers off at 215 au. The integrated flux, measured inside a circular mask with a radius of 4'', is $42.7 \pm 0.2 \text{ Jy km s}^{-1}$. (The integrated flux uncertainty is estimated with $\sqrt{\text{Area of mask}/\text{Area of beam}} \times \sigma$, where $\sigma = 3.8 \times 10^{-3} \text{ Jy km s}^{-1}$ is the rms of the unclipped integrated intensity map.) Taking systematic flux uncertainties into account

(≈10%), the integrated flux is consistent with previous ALMA and SMA measurements of ¹²CO $J = 3 - 2$ in the TW Hya disk (Andrews et al. 2012; Rosenfeld et al. 2012). The shortest projected baseline is 13.1 m, which corresponds to an angular scale of ≈14'' and should therefore adequately recover the large-scale structure in the ¹²CO emission.

We also imaged the line data without continuum subtraction to verify that the key emission features are not artifacts from continuum subtraction, which can create the appearance of line emission substructure if the line optical depth is high enough such that the total outgoing emission has little to no contribution from large dust grains settled near the midplane (e.g., Isella et al. 2016; Boehler et al. 2017). This effect is not to be confused with optically thick dust absorbing line emission and thereby creating the appearance of molecular emission gaps. In the TW Hya disk, the ¹²CO line intensity is substantially larger than that of the dust over many channels, so continuum subtraction does not have a large impact on the observed line emission morphology.

3.2.2. ¹²CO $J = 3 - 2$ Peak Brightness Temperatures

The ¹²CO peak brightness temperature map and its deprojected and azimuthally averaged radial profile are also shown in Figure 4. A peak brightness map is computed by taking the maximum value along the frequency axis for each pixel in the image cube and then converting to a brightness temperature using Planck’s law (rather than the Rayleigh–Jeans law, which is a poor approximation at these frequencies). Equivalently,

$$T_{\text{B,peak}}(x, y) = \max(T_{\text{B}}(\nu, x, y)), \quad (5)$$

where x and y are spatial coordinates and ν is the channel frequency. In practice, a peak intensity map produced from a single image cube will have minor artifacts tracing the emission boundaries in individual channels. To mitigate this issue, we follow the example of Christiaens et al. (2014) and produce three image cubes with the same channel width (0.25 km s⁻¹), but with the starting velocities offset by 0.1 km s⁻¹. Each image cube yields a peak brightness temperature map. Since the channelization artifacts are spatially offset from one another from map to map, a map with suppressed artifacts can be produced by taking the median value of each pixel from the individual maps.

A peak brightness temperature map for an optically thick line such as ¹²CO $J = 3 - 2$ provides an estimate of the gas temperature at the location where the line becomes optically thick, provided that the emission fills the beam. That assumption is valid for most of the disk, which is well resolved; the exception is the inner 10 au, where the peak brightness temperature dips. This feature is a consequence of an inclined Keplerian disk being observed at finite angular resolution. Because of the fast rotation of the inner disk, its emission is spread over a large number of channels, with only two narrow wedges contributing to the emission in any given channel (see also Schwarz et al. 2016, for a related discussion). Referring again to the Keplerian emission schematic in Figure 3, we see that any Gaussian beam placed over the disk center in a given channel would include regions of the disk contributing no emission.

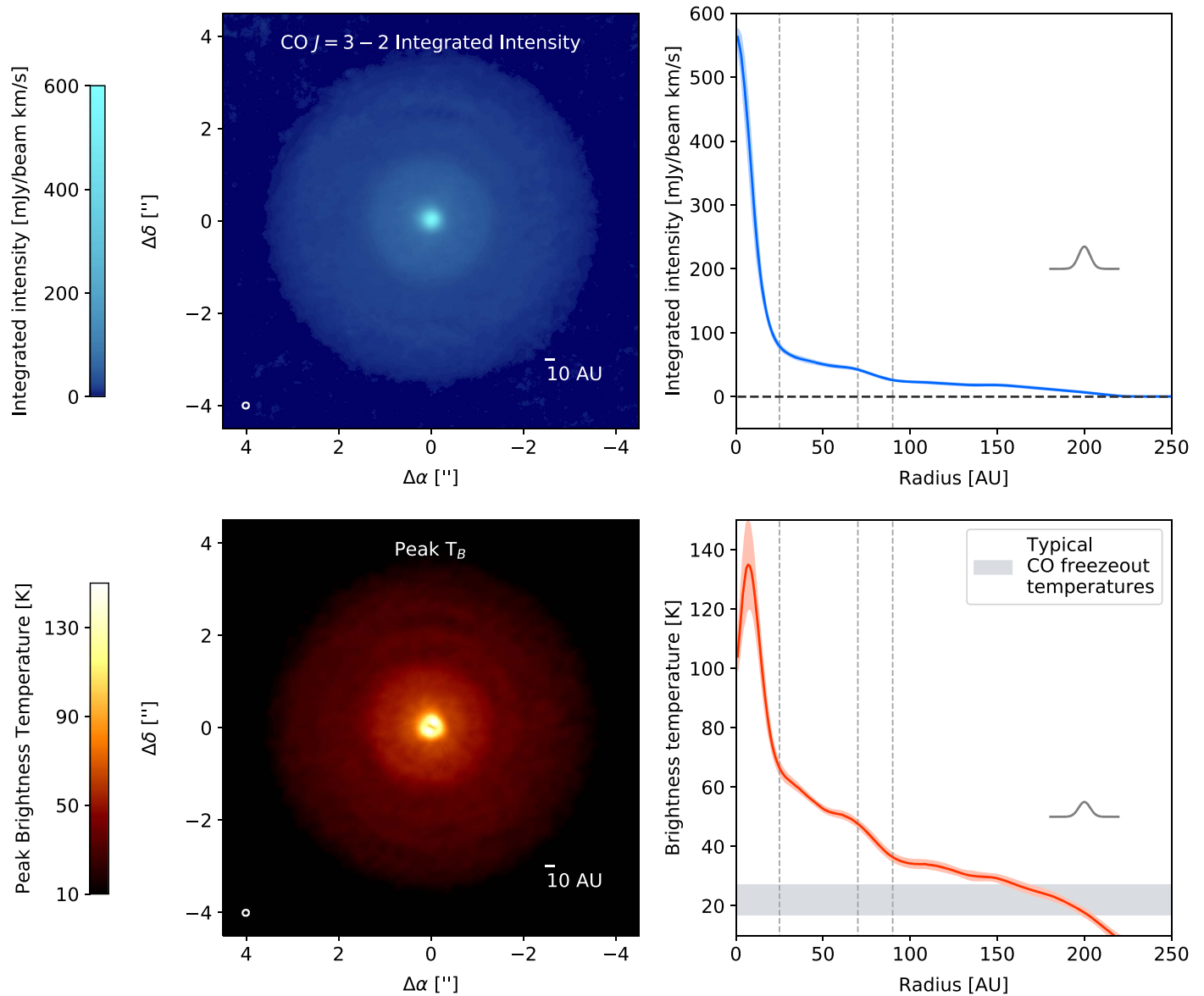


Figure 4. Top left: integrated intensity map of the $^{12}\text{CO } J=3-2$ line. The synthesized beam is shown in the lower left corner. Top right: deprojected and azimuthally averaged radial profile of the $^{12}\text{CO } J=3-2$ integrated intensity. The light-blue ribbon shows the 1σ scatter in each radial bin. The Gaussian profile shows the FWHM of the synthesized beam. Bottom left: peak brightness temperature map of $^{12}\text{CO } J=3-2$. Bottom right: deprojected and azimuthally averaged radial profile of the $^{12}\text{CO } J=3-2$ peak brightness temperature map. The light-orange ribbon shows the 1σ scatter in each radial bin. Vertical gray dashed lines mark the radial break in emission at 25 au, the shoulder at 70 au, and the second break at 90 au. Temperatures between 17 and 27 K are shaded gray to show CO freezeout temperatures that have been estimated for TW Hya (e.g., Qi et al. 2013 and Zhang et al. 2017).

The radial profile of the peak brightness temperature map shows an abrupt slope change at a radius of 25 au, a shoulder at 70 au, and another abrupt slope change at 90 au, corresponding to the features observed directly in the channel maps and integrated intensity map. The peak brightness temperatures between radii of 25 and 90 au range from ~ 70 to 35 K, which are about twice the value of the gas temperatures derived by Schwarz et al. (2016) from multiple transitions of the rarer ^{13}CO and C^{18}O isotopologues. Zhang et al. (2017) estimate that the $\text{C}^{18}\text{O } J=3-2$ flux contribution largely originates from within two gas scale heights of the midplane, in contrast to three to four scale heights for $^{12}\text{CO } J=3-2$. The difference in inferred gas temperatures for the isotopologues implies a steep vertical temperature gradient.

3.2.3. Comparison to Other CO Isotopologues

Since CO isotopologues become optically thick at different heights within the disk, they lend insight into the vertical structure. ALMA observations of the C^{18}O and $^{13}\text{CO } J=3-2$ transitions in the TW Hya disk have been presented in Schwarz et al. (2016), Nomura et al. (2016), and Zhang et al. (2017) at spatial resolutions ranging from $0''.3$ to $0''.5$. Although these resolutions are coarser than that of the ^{12}CO data, they are sufficient to reveal substructure. To facilitate comparisons, we reprocessed and combined archival ALMA observations of $^{13}\text{CO } J=3-2$ in the TW Hya disk. The reduction details and channel maps are provided in Appendix C. Whereas the integrated intensity maps were

presented in Schwarz et al. (2016) and Nomura et al. (2016), we now show the channel maps because they more clearly display the weak extended emission features.

The ^{13}CO and C^{18}O data in Schwarz et al. (2016), Nomura et al. (2016), and Zhang et al. (2017) show a bright core of emission, an annular gap at ≈ 40 au, and an outer emission ring peaking at ≈ 65 au. In the channel maps (see Figure 11 in Appendix C for ^{13}CO and Zhang et al. [2017] for C^{18}O), the annular gap creates central channel emission deficits that coincide spatially with the emission deficits noted for ^{12}CO . The deficits are more pronounced in ^{13}CO and C^{18}O because they are less optically thick than ^{12}CO ; a similar effect is observed in transition disks, where ^{13}CO and C^{18}O integrated intensity maps have much more prominent central cavities compared to ^{12}CO (e.g., van der Marel et al. 2015, 2016).

Like the ^{12}CO channel maps, the ^{13}CO channel maps in Figure 11 in Appendix C also show a steep drop-off in intensity at a radius of ≈ 90 au, followed by very faint emission extending out to ≈ 200 au, which is slightly less extended than the ^{12}CO emission. C^{18}O exhibits an outer emission ring that sharply drops off within a radius of 100 au (Zhang et al. 2017), but no emission is observed beyond this radius. The apparent differences between the isotopologues are likely primarily due to sensitivity limits, but they may also be partially due to selective photodissociation in the more tenuous outer disk (e.g., Miotello et al. 2014).

Based on integrated flux ratios, ^{12}CO and ^{13}CO $J = 3 - 2$ are known to have high optical depths in the TW Hya disk (Qi et al. 2013). However, it is also instructive to determine whether ^{12}CO is still optically thick beyond a radius of 100 au, where the emission becomes comparatively weak. As a crude check, we measure the $^{12}\text{CO}/^{13}\text{CO}$ integrated flux ratio using an annulus with an inner radius of $1''.7$ (101 au) and an outer radius of $3''.6$ (214 au). Inside this annulus, the $^{12}\text{CO}/^{13}\text{CO}$ flux ratio is ≈ 20 , which is smaller than the interstellar $^{12}\text{CO}/^{13}\text{CO}$ abundance ratio of ≈ 69 (e.g., Wilson 1999) and suggests that ^{12}CO remains optically thick in the outer disk. The $^{12}\text{CO}/^{13}\text{CO}$ ratio in the outer disk may be even higher than the interstellar medium (ISM) ratio owing to less effective ^{13}CO self-shielding (e.g., Visser et al. 2009; Miotello et al. 2014), in which case the flux ratio still implies that ^{12}CO is optically thick.

4. ^{12}CO Radiative Transfer Modeling

4.1. Overview

To explore possible origins for the ^{12}CO emission substructure, we perform radiative transfer calculations based on several sets of parametric structure models. Given the complex details visible at high resolution, as well as the large computational cost of synthesizing the image cubes, our aim in this work is not to present an optimal model, but to provide guidance for which physical and chemical mechanisms would plausibly yield the key emission features noted in Section 3. Similar modeling approaches have been favored for ALMA observations of molecular line emission in a number of works (e.g., Rosenfeld et al. 2012, 2013; Isella et al. 2016; Öberg et al. 2017) because of the flexibility offered in directly specifying temperature structures and molecular abundances to explore particular emission features of interest. An alternative approach is thermochemical disk modeling, which computes dust and gas structures and molecular abundances in a physically self-consistent manner via numerical

codes such as ProDiMo (Woitke et al. 2009) or DALI (Bruderer et al. 2012), although such an approach is also subject to uncertainties in the values adopted for parameters such as dust opacities or reaction rates (e.g., Vasyunin et al. 2008; Kamp et al. 2017). The parametric and thermochemical approaches are ultimately complementary; physical models guide the setup of parametric models, the results of which then motivate additional physical modeling (e.g., Andrews et al. 2012; Qi et al. 2013; Birnstiel & Andrews 2014; van't Hoff et al. 2017).

Because continuum subtraction did not appear to introduce artifacts to the ^{12}CO image cubes, we model the continuum-subtracted line emission rather than line+continuum, which would require a number of additional assumptions and free parameters to model the dust. As discussed in Boehler et al. (2017), continuum subtraction tends to remove a larger fraction of ^{13}CO and C^{18}O line emission because these lines are less bright overall but are still optically thick in the inner disk. Since a detailed physical model for the continuum would likely be necessary to construct a CO model consistent with all isotopologue data, we focus on modeling ^{12}CO $J = 3 - 2$ only in the present paper, and we defer dust modeling and multiline fitting to future work.

Perhaps the most straightforward explanation of the ^{12}CO emission features is that they trace an initial sharp drop in the CO column density, which then rebounds in the outer disk. Such a column density profile has been inferred previously based on observations of less optically thick CO isotopologues in the TW Hya disk (Nomura et al. 2016; Schwarz et al. 2016; Zhang et al. 2017). Hence, our fiducial ^{12}CO model is motivated by the C^{18}O $J = 3 - 2$ model presented in Zhang et al. (2017). We also construct a model with a monotonically decreasing CO column density profile to demonstrate how its emission features differ from the fiducial model. We then examine the impact of our assumptions about CO freezeout. Finally, we briefly consider how assumptions about the form of the temperature structure affect inferences about the CO column density profile.

We make several assumptions common to all models. Because there are no clear azimuthal asymmetries in the ALMA data, all the models are axisymmetric and specified in cylindrical coordinates. After some experimentation, the inclination and position angle were fixed to 5° and 152° , respectively. Local thermal equilibrium is assumed for calculating the intensity of ^{12}CO $J = 3 - 2$ because its critical density ($\sim 10^4 \text{ cm}^{-3}$) is small relative to typical disk gas densities (e.g., Pavlyuchenkov et al. 2007).

To first order, the gas velocity field is that of a thin Keplerian disk in which the stellar mass greatly exceeds the disk mass:

$$\begin{cases} v_r = v_z = 0 \\ v_\phi = \sqrt{\frac{GM_*}{r}}. \end{cases} \quad (6)$$

As in Zhang et al. (2017), we fix the microturbulent line broadening parameter to $a_{\text{turb}} = 0.01 \text{ km s}^{-1}$, but we note that this value was motivated by general disk theory rather than from a direct measurement, and in practice this parameter likely varies spatially. The value of this parameter is not well established—estimates for the TW Hya disk have been disparate owing to differences in methodology and limitations in instrumental resolution and precision (Hughes et al. 2011; Teague et al. 2016). The turbulence values that have been estimated for the TW Hya disk are smaller than the spectral

resolution of our observations, limiting their utility in constraining turbulence independently. In terms of modeling line emission, turbulence is highly degenerate with the thermal structure (see also Simon et al. 2015, for a more detailed exploration). Holding all other parameters equal, increasing the turbulent broadening parameter by a factor of 10 (bringing it up to the higher values estimated by Teague et al. 2016) makes the emission features “blurrier” and “fills in” the central emission deficits in the channel maps, but the difference is modest and does not qualitatively change our interpretation of the CO observations.

The largest projected velocities where ^{12}CO emission is detected ($\pm 4.75 \text{ km s}^{-1}$ from the systemic velocity) suggest that there is gas within at least a few tenths of an au from the central star, assuming $v_{\text{proj}} = \sqrt{\frac{GM_*}{r}} \sin(i)$. In the absence of more precise information about the gas inner radius, we set R_{in} to 0.05 au, roughly the inferred location of the inner dust rim (Eisner et al. 2006). The outer radius R_{out} is set to 215 au, based on the extent of ^{12}CO emission above the 3σ level in the channel maps.

Between the inner and outer radii, we assume that the vertical distribution of the gas is approximated by a Gaussian with a standard deviation $H_{\text{mid}}(r)$, where

$$H_{\text{mid}}(r) = \sqrt{\frac{k_B T_{\text{mid}}(r) r^3}{\mu_{\text{gas}} m_{\text{H}} GM_*}} \quad (7)$$

is the gas pressure scale height, $T_{\text{mid}}(r)$ is the midplane temperature, $\mu_{\text{gas}} = 2.37$ is the mean mass for a gas particle, and m_{H} is the mass of atomic hydrogen. We therefore express the ^{12}CO number density as

$$n_{\text{CO}}(r, z) = p(T(r, z)) \times \frac{N(r)}{\sqrt{2\pi} H_{\text{mid}}(r)} \times \exp\left[-0.5 \left(\frac{z}{H_{\text{mid}}(r)}\right)^2\right]. \quad (8)$$

$N(r)$ is a scaling factor that simplifies to the ^{12}CO column density profile in the case where $p(T) = 1$ everywhere (e.g., in the absence of freezeout). The step function $p(T)$ accounts for CO freezeout, such that $p = 1$ for gas temperatures above some freezeout temperature T_{frz} and $p = 10^{-6}$ everywhere else. This procedure, similar to the treatment in Qi et al. (2008), divides the disk into a warm molecular layer with abundant CO and a cold midplane layer where freezeout depletes gas-phase CO. In general, UV photodissociation sets the upper boundary of the CO distribution and plays a role in setting the outer boundary (e.g., Aikawa & Herbst 1999). Because ambiguities in the gas and grain size distribution (see Section 5) render explicit calculations of the photodissociation boundary difficult, we elect to parameterize the CO distribution directly.

The radiative transfer code RADMC-3D¹² (Dullemond 2012) is used to compute the ^{12}CO level populations and perform the ray tracing to produce model image cubes. The parametric

Table 2
Parameter Values for ^{12}CO Models

Parameter	Fiducial	Freezeout Only	No Freezeout	Perturbed Temperature
R_{in} (au)	0.05	0.05	0.05	0.05
R_{out} (au)	215	215	215	215
γ	0.9	0.9	0.9	0.9
N_{CO} (cm^{-2})	3×10^{19}	3×10^{19}	3×10^{19}	7.5×10^{17}
R_1 (au)	15	...	15	15
R_2 (au)	70	...	70	70
A	3	...	3	...
f	0.025	...	0.025	...
σ_{in}	12	...	12	...
σ_{out}	6	...	6	...
$T_{\text{mid},10}$ (K)	40	40	40	40
$T_{\text{atm},10}$ (K)	125	125	125	125
q	0.47	0.47	0.47	0.47
δT	1.6
B	0.15
$\sigma_{T_{\text{in}}}$	15
$\sigma_{T_{\text{out}}}$	6
T_{frz} (K)	27	27
a_{urb} (km s^{-1})	0.01	0.01	0.01	0.01

expressions for the temperature, gas velocity, and ^{12}CO number density are evaluated at 400 logarithmically spaced radial bins from 0.05 to 400 au and at 100 logarithmically spaced polar angle bins from 0 to $\pi/2$ in a spherical coordinate system (note that the grid points are converted to cylindrical coordinates before the expressions are evaluated, and mirror symmetry is assumed for the upper and lower halves of the disk). The molecular data inputs for the radiative transfer are obtained from the LAMDA database (Schöier et al. 2005). To account for the effects of nonzero channel widths on the observed spatial distribution of the line emission, the model image cubes are synthesized at a velocity resolution of 0.05 km s^{-1} and subsequently averaged to a resolution of 0.25 km s^{-1} to match the observations. The `vis_sample` package¹³ (Czekala et al. 2015; Loomis et al. 2017) is used to sample the radiative transfer images at the same spatial frequencies as the data in order to produce model visibilities, which are then imaged with the same procedure described in Section 2.

The model parameters are listed in Table 2, and the gas temperatures and ^{12}CO number and column densities for each model are plotted in Figure 5. Channel maps made from the model visibilities are shown in Figure 6, beneath the corresponding channels from the observations. To highlight some details of the models, insets of the central three channels and radial profiles of the peak brightness temperature maps are shown in Figure 7.

4.2. The Fiducial Model

The parameterization and values for the fiducial model are motivated by the C^{18}O column density profile derived in Zhang et al. (2017)—the CO column density decreases sharply in the inner disk and then features a secondary peak in the outer disk. Functionally, this is specified by setting the scaling factor for

¹² <http://www.ita.uni-heidelberg.de/~dullemond/software/radmc-3d/>

¹³ Version used in this work available at https://github.com/AstroChem/vis_sample/tree/j. General version available at https://github.com/AstroChem/vis_sample.

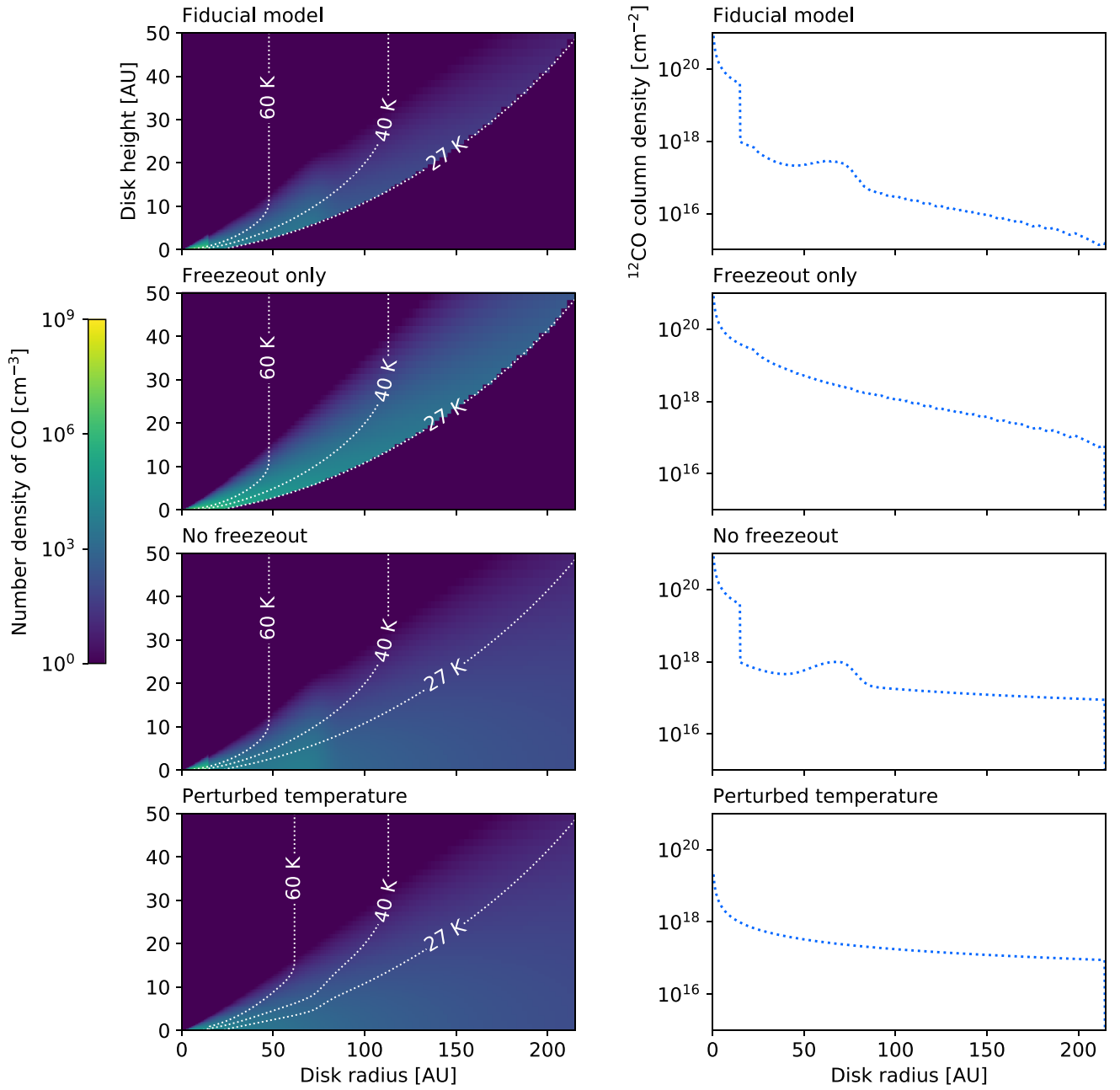


Figure 5. Plots of the four parametric model structures used as radiative transfer inputs. Left: ^{12}CO number density color maps with isotherms overlotted as dashed white lines. Right: corresponding ^{12}CO gas column densities for each model.

the number density to be

$$N(r) = N_{\text{CO}} \left(\frac{r}{20 \text{ au}} \right)^{-\gamma} \times f_1(r) \times f_2(r). \quad (9)$$

Here $f_1(r)$ is a factor setting the radial location and degree of the column density drop in the inner disk,

$$f_1(r) = \begin{cases} 1, & r < R_1 \\ f, & r \geq R_1 \end{cases}, \quad (10)$$

and $f_2(r)$ sets the shape of the secondary bump in the ^{12}CO column density profile such that

$$f_2(r) = \begin{cases} 1 + A \exp\left(-\frac{(r-R_2)^2}{2\sigma_{\text{in}}^2}\right), & r < R_2 \\ 1 + A \exp\left(-\frac{(r-R_2)^2}{2\sigma_{\text{out}}^2}\right), & r \geq R_2. \end{cases} \quad (11)$$

The asymmetric Gaussian shape of the secondary bump is motivated by the shallow slope of the CO integrated intensity radial profile inward of 70 au and the much steeper slope outside of 70 au, although other parameterizations may achieve similar effects. N_{CO} is set to $3 \times 10^{19} \text{ cm}^{-2}$, assuming that the

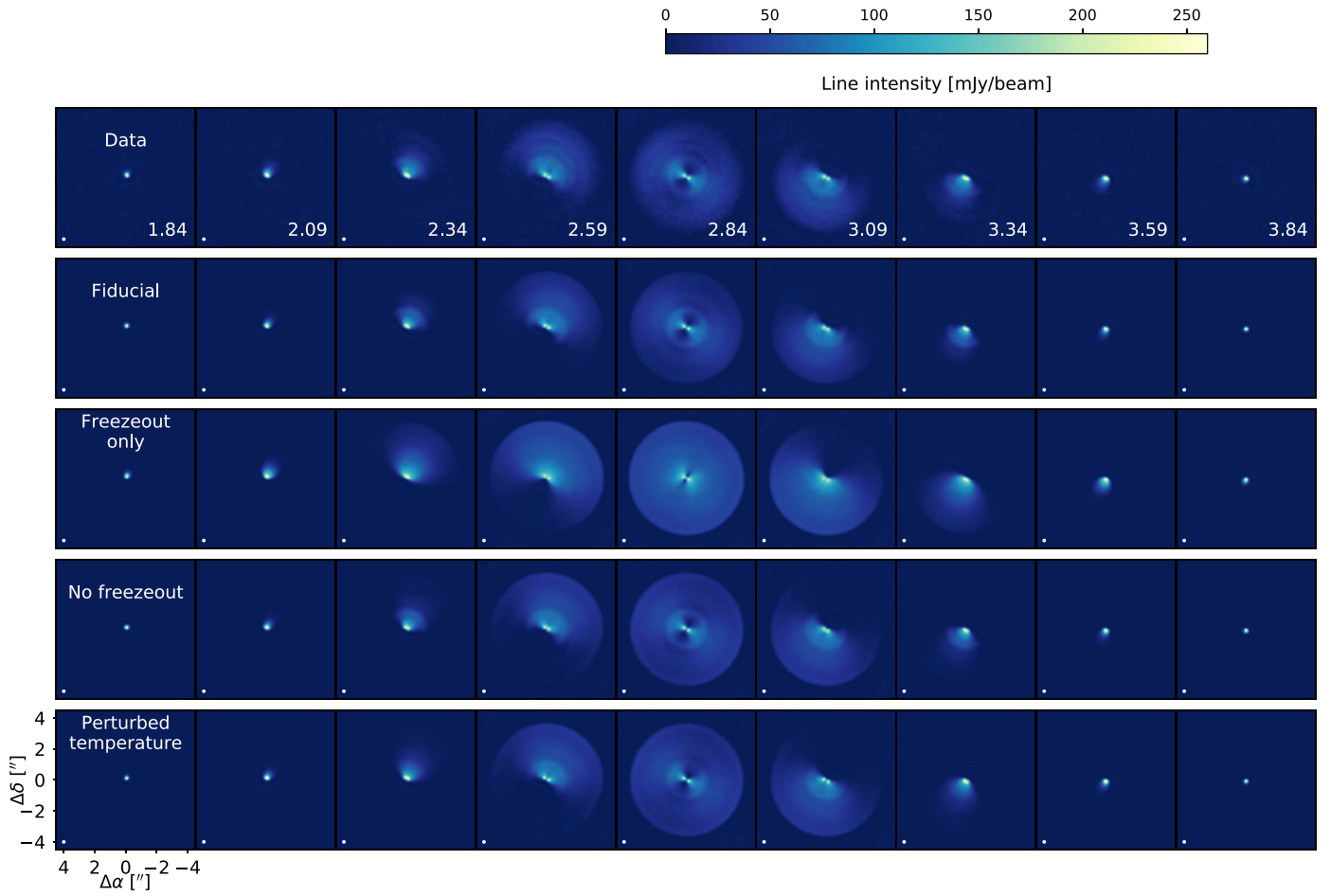


Figure 6. Central channels of the $^{12}\text{CO } J = 3 - 2$ observations, compared with model channel maps. Synthesized beams are drawn in the lower left corner of each panel. The LSR velocity (km s^{-1}) is shown in the lower right corner of each panel in the first row. The offset from phase center is marked in arcseconds in the lower left panel.

^{12}CO -to- C^{18}O abundance ratio follows the local ISM value of ~ 500 (e.g., Wilson 1999). The model parameter values are listed in Table 2.

Because LTE is assumed, the absolute ^{12}CO number density distribution is directly input into RADMC-3D without requiring the underlying gas distribution to be specified. The parameterization for ^{12}CO in Equations (8) and (9) can therefore be viewed in two equivalent ways:

1. The fractional CO abundance, X_{CO} , is constant in the warm molecular layer, and perturbations in the gas surface density profile govern the radial variation in the ^{12}CO column density profile. An “unperturbed” surface density profile is assumed to follow a power law, as outlined in Lynden-Bell & Pringle (1974) for a viscous disk. More colloquially, these perturbations might be referred to as an annular gap and ring in the gas distribution.
2. The gas surface density profile follows a standard power law, and radially varying CO depletion (i.e., reductions in X_{CO}) in the warm molecular layer creates the radial variations in the ^{12}CO column density profile.

The temperature structure is modeled using the vertical gradient prescription presented in Dartois et al. (2003) and

Andrews et al. (2012):

$$T(r, z) = \begin{cases} T_{\text{atm}}(r) + (T_{\text{mid}}(r) - T_{\text{atm}}(r)) \cos^4\left(\frac{\pi z}{2z_q}\right) & z < z_q \\ T_{\text{atm}}(r) & z \geq z_q \end{cases} \quad (12)$$

where

$$T_{\text{atm}}(r) = T_{\text{atm},10} \left(\frac{r}{10 \text{ au}}\right)^{-q}, \quad (13)$$

$$T_{\text{mid}}(r) = T_{\text{mid},10} \left(\frac{r}{10 \text{ au}}\right)^{-q}, \quad (14)$$

and

$$z_q = 4H_{\text{mid}}(r). \quad (15)$$

Zhang et al. (2017) employ a vertically isothermal model, assuming that C^{18}O emits at the midplane temperature. In contrast, ^{12}CO becomes optically thick well above the midplane, requiring the adoption of a vertical temperature gradient. We set $T_{\text{mid},10} = 40 \text{ K}$ and $q = 0.47$ based on the midplane temperature derived in Zhang et al. (2017). $T_{\text{atm},10}$ is less constrained; we choose a value of 125 K such that the

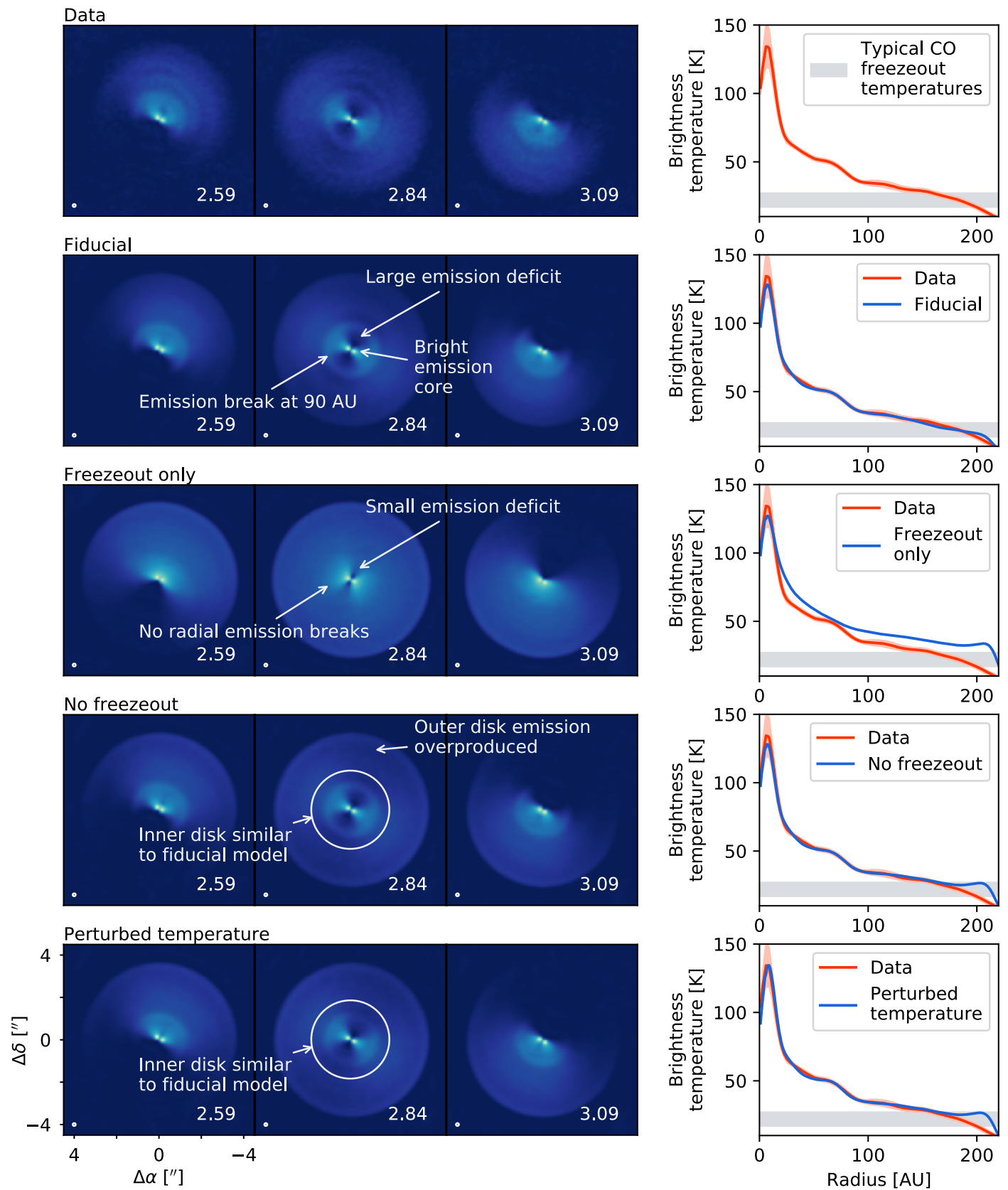


Figure 7. Insets of the three central channels for each model to highlight the substructures, along with the corresponding radial profile of the peak brightness temperature map.

spatially integrated fluxes of the channels at the systemic velocity for the observations and fiducial model are within 5% of one another. This value is broadly in line with the detailed temperature structures computed from fitting the SED (e.g., Cleves et al. 2015; Kama et al. 2016). The consequences of our assumptions about the temperature structure are discussed later.

The fiducial model images, shown in Figures 6 and 7, reasonably reproduce the three key features of the observed channel maps—the sharp drop in the ^{12}CO column density at $r = 15$ au creates the bright “hourglass” emission core and the nearby emission deficits in the central channels, and the secondary bump in the column density creates the emission shoulder at $r \approx 70$ au and the radial intensity break at ≈ 90 au. Whereas specifying a sharp drop in the CO column density creates a clear annular gap in models of C^{18}O emission (Zhang et al. 2017), the impact is more subtle in ^{12}CO emission owing to its much higher optical depth. In the optically thin limit, intensity scales almost linearly with column density. In contrast, for optically thick ^{12}CO , altering the number density changes the height and therefore the temperature of its emitting surface in the disk, which yields emission substructure. It should be noted that the drop in the column density at $r = 15$ au reproduces the break in the emission profile slope at $r \approx 25$ au because the beam smears out the radial change in intensity.

The model slightly underestimates the line intensity in the inner few au of the disk. This may be due to complexities in the vertical structure that are unaccounted for in the model, deviations from Keplerian rotation in the inner disk (Rosenfeld et al. 2012), or the slightly differential rotation associated with a geometrically thick disk (e.g., Rosenfeld et al. 2013). While our simple models are aimed at elucidating features 15 au and beyond, the effect of these secondary considerations on the inner disk would be interesting to explore in future work.

In the outer disk past a radius of 90 au, there are additional faint arcs visible in the central three channels even though the surface density profile is smooth at these radii. These appear to be artifacts from imaging the visibilities with CLEAN. Similar faint arcs appear in the outer disk emission in the ^{12}CO observations and may be imaging artifacts as well. However, since the arcs in the data persist with different choices of imaging parameters and do not exactly match the artifacts in the model images, it is difficult to say for certain whether there is any genuine physical origin for these features.

4.3. A Freezeout-only Model

While the fiducial model illustrates that substructure in the CO column density profile is compatible with the observed ^{12}CO emission, it does not by itself demonstrate that substructures are *necessary* to create the observed emission features. Given the high optical depth of $^{12}\text{CO } J = 3 - 2$, it is not intuitive that column density substructure would have a visible impact on its emission morphology. It is therefore instructive to compare the fiducial model with a “freezeout-only” model, where the ^{12}CO column density profile decreases monotonically from the disk center and no depletion occurs in the warm molecular layer.

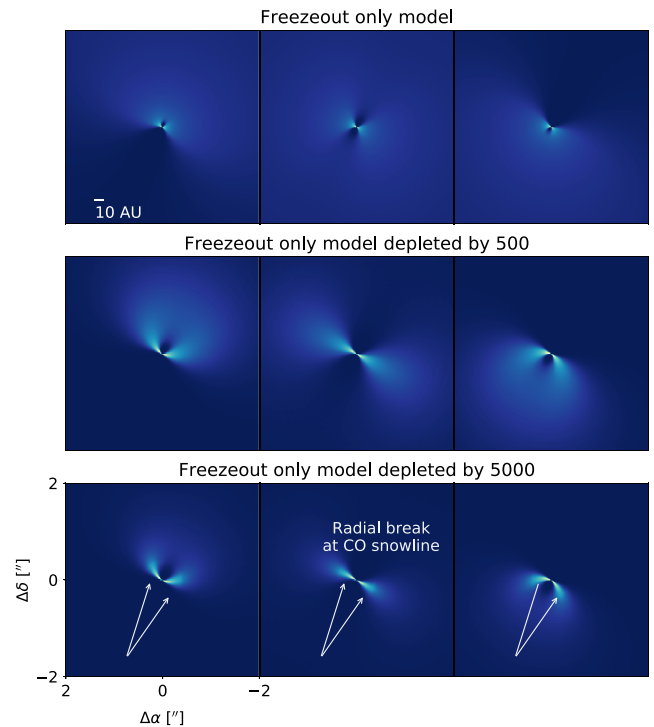


Figure 8. Comparison of the central three channels of the RADMC-3D “freezeout-only” images (zoomed in to the inner $2''$ of the disk) with models where N_{CO} is reduced by a factor of 500 and 5000, respectively. Only the model depleted by a factor of 5000 shows a radial intensity break corresponding to the location of the CO snowline.

The ^{12}CO number density scaling factor is now

$$N(r) = N_{\text{CO}} \left(\frac{r}{20 \text{ au}} \right)^{-\gamma}, \quad (16)$$

i.e., it is an extrapolation of the profile in the inner disk of the fiducial model. The “freezeout-only” model is otherwise specified in the same fashion as the fiducial model. This “freezeout-only” model is similar to the parameterization that has been used to fit CO emission in a number of protoplanetary disks observed at coarser angular resolution (e.g., Andrews et al. 2012; Williams & Best 2014; Flaherty et al. 2015).

The resulting model channel maps, shown in Figures 6 and 7, differ dramatically from those of the observations and fiducial model. The failure of the “freezeout-only” model to reproduce the key features of the observations indicates that these features are not artifacts resulting from sparse uv coverage or of the deconvolution algorithm, but reflect the structure of the disk itself. No intensity break appears at a radius of 90 au, since the surface density profile is smooth there. While a bright emission core is present owing to the high temperatures of the inner disk, the core is not as sharply defined as in either the observations or the fiducial model. Though emission deficits near the center of the disk are visible at the systemic velocity, they are substantially smaller than the ones in the observations and fiducial model. As remarked on in Section 2, emission deficits at those locations are expected for inclined disks in Keplerian rotation, but the discrepancy between the scale of the deficits for the fiducial and “freezeout-only” models suggests that disk orientation alone does not explain the observed emission morphology—an abrupt change in the CO column density and/or temperature profile has

to occur near $r \approx 15$ au to simultaneously create the bright inner emission core and adjacent emission deficits.

For this “freezeout-only” model, the midplane CO snowline does not create a marked intensity break because the ^{12}CO emission is too optically thick. N_{CO} , which sets the overall scale of the column density profile, has to be reduced by a factor of several thousand for the CO snowline to become visible in the images generated by RADMC-3D, and even then the effect is subtle (see Figure 8). In contrast, the fiducial model only invokes a factor of 40 reduction in the ^{12}CO column density at a radius of 15 au to create emission substructure by lowering the CO-emitting height. While CO column densities are not well constrained by ^{12}CO , the value of N_{CO} chosen for the unreduced “freezeout-only” model is based on column density estimates from observations of C^{18}O , which has much lower optical depth (Zhang et al. 2017). Since it is unlikely that C^{18}O column densities have been overestimated by several orders of magnitude for the TW Hya disk, severely reducing N_{CO} to decrease the optical depth of ^{12}CO does not seem to be a viable route for reproducing the observed ^{12}CO emission morphology.

4.4. A Model with No Freezeout

While the fiducial model adopts a CO freezeout temperature of 27 K to be consistent with the C^{18}O model from Zhang et al. (2017), Qi et al. (2013) previously advocated for a freezeout temperature of 17 K in the TW Hya disk. In practice, CO desorption occurs at various temperatures over this range, depending on the substrate (e.g., Sandford & Allamandola 1988; Collings et al. 2003; Fayolle et al. 2016). Hence, it is worthwhile to examine how the model emission depends on the treatment of CO freezeout. To illustrate how an extreme change in the CO freezeout specification could look, we produce a “no-freezeout” model by using a CO number density structure in which $p(T) = 1$ everywhere in Equation (8). In all other respects, the “no-freezeout” model is identical to the fiducial model.

The resulting model channel maps are shown in Figure 6. Past $r \approx 150$ au, the model images overproduce emission in comparison with the observations and the fiducial model, but the key features of the ^{12}CO emission (i.e., the bright core, the nearby emission deficits in the central channels, and the break in intensity at 90 au) look similar. This suggests that the ^{12}CO emission morphology in the inner disk is not sensitive to differences in assumptions about CO freezeout.

One could perhaps devise a colder temperature structure that removes so much gas-phase CO that the optical depth of ^{12}CO is low enough to reveal its midplane snowline. However, this possibility for TW Hya can be ruled out by the ^{12}CO peak brightness temperature map in Figure 4. Within a radius of 100 au, the peak brightness temperatures are well above the range of expected CO freezeout temperatures, indicating that the ^{12}CO emitting surface is at a height much warmer than the snow surface and therefore does not trace the onset of freezeout in the midplane.

4.5. A “Perturbed Temperature” Model

The models we have presented so far sought to reproduce the observed ^{12}CO emission morphology by shifting the CO emitting height through surface density substructures. An alternative route is to modify the disk temperature structure

directly. The temperature structure used for the previous models has been relatively simple, with the radial temperature dependence following a standard power law for a fixed height. However, models from several works suggest that the TW Hya temperature structure could be much more complex. First, scattered-light observations of the TW Hya disk show multiple annular gaps (e.g., Debes et al. 2013; Akiyama et al. 2015; Rapson et al. 2015; van Boekel et al. 2017). Relative to a smooth disk model, the troughs of gaps have lowered temperatures owing to shadowing from the interior wall of the gap, while the far walls of gaps receive more stellar radiation and therefore feature elevated temperatures (e.g., Jang-Condell & Turner 2012, 2013). Additional cooling of the gas may occur within the gap if dust densities decrease to the point where the gas and dust temperatures are no longer coupled via collisions (Facchini et al. 2017b). Second, inward radial drift of larger solids in disks may create radial temperature inversions; Cleeves (2016) discusses how radial drift reduces dust optical depths in the outer disk and allows stellar radiation to penetrate deeper in the disk, while Facchini et al. (2017a) suggest that radial drift allows the outer disk to be heated more efficiently because the remaining small grains are lofted upward and receive more stellar illumination.

To illustrate how thermal and density variations can create similar emission patterns, we construct a model that has a smooth CO column density profile. The bright inner core of emission and the intensity break at 90 au seen in the data are then reproduced by increasing the temperatures in these regions relative to the fiducial model. The ^{12}CO number density scaling factor $N(r)$ is again described by a power law, i.e., Equation (16). N_{CO} is set to $7.5 \times 10^{17} \text{ cm}^{-2}$ such that the ^{12}CO column density profile matches that of the disk outside 15 au in the “no-freezeout” model, excluding the secondary column density bump. In order to keep the column density profile smooth, CO freezeout is ignored in this model. As shown in the “no-freezeout” model, the treatment of CO freezeout does not have a noticeable effect on the inner 150 au of the disk, which is where the substructure is observed.

The modified temperature structure is

$$T_{\text{perturbed}}(r, z) = T_{\text{fiducial}} \times g_1(r) \times g_2(r). \quad (17)$$

The prescription for $g_1(r)$ creates a hot inner disk, similar to a TW Hya model from Rosenfeld et al. (2012):

$$g_1(r) = \begin{cases} \delta T & r < R_1 \\ 1 & r \geq R_1. \end{cases} \quad (18)$$

Further, $g_2(r)$ creates a secondary warm region in the outer disk:

$$g_2(r) = \begin{cases} 1 + B \exp\left(-\frac{(r-R_2)^2}{2\sigma_{\text{in}}^2}\right), & r < R_2 \\ 1 + B \exp\left(-\frac{(r-R_2)^2}{2\sigma_{\text{out}}^2}\right), & r \geq R_2. \end{cases} \quad (19)$$

Parameters $g_1(r)$ and $g_2(r)$ are the temperature analogs to $f_1(r)$ and $f_2(r)$, the factors setting the CO column density drop in the inner disk and secondary bump in the outer disk for the fiducial model. While these parameterizations aim to reproduce some of the general characteristics of the thermal variations derived for disk models that incorporate annular gaps or radial drift, simplifications are also made (e.g., the temperature step

function in the inner disk) in order to allow for a more direct comparison with the fiducial model. The model parameters are listed in Table 2.

As shown in Figures 6 and 7, the emission morphology within a radius of 150 au is quite similar to the observations. As expected for optically thick CO, the relative variations in the thermal profile necessary to create emission substructure are much smaller than the variations that would be required in the column density profile. Whereas the key observed emission features were reproduced in the fiducial model through a factor of 40 decrease in the CO column density at 15 au and then a secondary bump by a factor of a few in the outer disk, the “perturbed temperature” model only boosts temperatures by 60% ($\delta T = 1.6$) in the inner disk and by 15% ($B = 0.15$) at the peak of the secondary ring relative to the fiducial model. The width of $g_2(r)$, setting the secondary bump in the temperature profile, is somewhat wider than that of $f_2(r)$, which sets the secondary bump in the CO column density profile in the fiducial model. Since the temperature profile declines more steeply with radius than the CO column density profile, the temperature has to be increased over a wider region to reproduce the same emission bump that is generated by an increase in the CO column density.

While a smooth CO surface density profile is used to isolate the effects of temperature in creating emission substructure, this model is not physically self-consistent. Although the “perturbed temperature” model suggests that the depletion and enhancement factors in the CO surface density profile may be more modest than those used for the fiducial model, the mechanisms that have been proposed for creating localized thermal variations should still yield variations in the CO column density. For example, Jang-Condell & Turner (2012) find that a disk gap with the surface density reduced by a factor of 6 can yield thermal variations on the order of 25% compared to a smooth disk. For thermal variations mediated by radial drift, heating of the outer disk would promote CO ice desorption, thereby creating a secondary CO column density bump. Hence, while the CO emission substructure may be largely a temperature effect from the radiative transfer point of view, they would still ultimately signify the presence of surface density substructure.

5. Discussion

5.1. Possible Origins of the CO Emission Features

Our fiducial model indicates that the emission morphology of ^{12}CO in the TW Hya disk can be reasonably reproduced with a steep decrease in the ^{12}CO column density at a radius of ≈ 15 au, followed by a secondary peak at a radius of ≈ 70 au. To evaluate what scenarios are likely to have created these column density variations, we consider the ^{12}CO results in the context of other observations of the TW Hya disk, as well as physical and chemical modeling results from the literature.

5.1.1. Midplane CO Freezeout

Estimates for the TW Hya disk’s midplane CO snowline location range from 11 to 33 au (Qi et al. 2013; Nomura et al. 2016; Schwarz et al. 2016; Powell et al. 2017; van’t Hoff et al. 2017; Zhang et al. 2017), so it is natural to consider whether the apparent steep drop in ^{12}CO column density at a radius of 15 au is related. Indeed, several of the aforementioned CO snowline estimates are based on observations of a dip in the

C^{18}O emission profile at a radius (22 au) close to where we infer a ^{12}CO column density drop.

As noted in our analysis of the ^{12}CO brightness temperatures in Section 4.4, the ^{12}CO emission appears to originate well above the CO snow surface, which is in line with typical assumptions about disks. This implies that the inferred column density drop at $r = 15$ au and the bump at $r = 70$ au do not directly trace the onset of CO freezeout in the midplane. Because similar emission features are observed in ^{13}CO and $\text{C}^{18}\text{O } J = 3 - 2$ (Nomura et al. 2016; Schwarz et al. 2016; Zhang et al. 2017), which emit from different heights in the disk owing to their lower optical depths, we argue that the line observations together likely trace CO depletion or gas density reductions occurring throughout the vertical extent of the warm molecular layer, not just near the midplane. Consequently, while the aggregate evidence indicates that the midplane CO snowline does lie somewhere between 11 and 33 au in the TW Hya disk, we advise general caution in using CO isotopologue observations to infer the CO snowline location.

5.1.2. Gas Surface Density Substructures

Optically thick ^{12}CO emission does not directly constrain the molecular gas distribution of the TW Hya disk, but the distribution of sub-micron-sized dust grains has been used as a proxy because small grains are usually well coupled to gas (Debes et al. 2013; Akiyama et al. 2015; Rapson et al. 2015; van Boekel et al. 2017). Most recently, van Boekel et al. (2017) presented SPHERE scattered-light observations showing wide radial depressions at ≈ 23 and ≈ 94 au, which they interpreted as tracing gas surface density variations. These depressions overlap with where we infer steep ^{12}CO column density decreases in our fiducial model, which may indicate that the ^{12}CO emission is also following gas surface density variations.

Nonetheless, there are at least two apparent discrepancies between the inferred gas surface density profile from van Boekel et al. (2017) and the inferences we have made regarding the CO distribution in the TW Hya disk. First, their inferred gas surface density profile attains a local maximum just outside $r = 100$ au, whereas none of the CO isotopologue observations show an obvious rise in intensity outside this radius. Complementary chemical modeling of double CS emission rings by Teague et al. (2017) indicates that their observations are best reproduced by a gas surface density depression similar to the one inferred by van Boekel et al. (2017) at a radius of 94 au. One possible resolution to this discrepancy is that the small dust grains become less well coupled to the gas in the more tenuous upper layers of the cold outer disk. Alternatively, CO traces the gas surface density decrease into the 94 au gap but does not rise again with the gas surface density owing to more substantial CO freezeout in the outer disk.

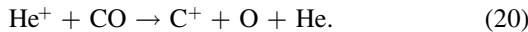
Second, the relative amplitudes of the gas surface density variations inferred by van Boekel et al. (2017) range roughly from 45% to 80%. The Zhang et al. (2017) model, which motivated our fiducial model, derived a C^{18}O column density drop by an order of magnitude in the inner disk and then an increase by a factor of a few to create the secondary ring. While our “perturbed temperature” model provides an example of how the ^{12}CO column density variations needed to reproduce the observations are sensitive to the prescribed temperature structure, column density estimates from the rarer and therefore less optically thick isotopologues should be more robust.

On the other hand, temperature, dust surface density, and dust opacities are degenerate with one another, so more stringent constraints on the temperature structure of the TW Hya disk would be essential to determine whether more extreme gas surface density variations are also compatible with the scattered-light data. In the meantime, we do not rule out the possibility that substructure in the underlying gas disk at least partially contributes to the observed CO emission morphology.

5.1.3. CO Depletion in Warm Gas

Another possibility to consider is that the features are due to spatial variations of X_{CO} in warm gas: X_{CO} drops by one to two orders of magnitude near 15 au and then rises by a factor of a few in the outer disk before decreasing again, creating the secondary CO column density bump peaking at ≈ 70 au. While several studies have suggested that warm gas in the TW Hya disk is CO depleted by one to two orders of magnitude relative to the ISM (Favre et al. 2013; Kama et al. 2016; Nomura et al. 2016; Schwarz et al. 2016; Powell et al. 2017), the new high angular resolution ALMA observations provide additional insight into how the CO distribution varies radially.

Destruction of CO by He^+ is an oft-proposed mechanism for CO depletion in disks (e.g., Favre et al. 2013; Nomura et al. 2016; Yu et al. 2016). Stellar X-rays ionize helium, which then reacts with CO (Herbst & Klemperer 1973; Bergin et al. 2014):



Much of the C^+ is thought to be incorporated back into CO, but alternative pathways incorporating C^+ into CO_2 , hydrocarbons, and complex oxygen-bearing molecules can still lead to significant CO depletion over timescales of several million years (e.g., Aikawa et al. 1997; Bergin et al. 2014; Yu et al. 2016).

Alternatively, CO depletion in the warm molecular layer could be directly tied to CO freezeout deeper in the disk. Xu et al. (2017) presented “turbulent-diffusion mediated CO depletion” models demonstrating that if small dust grains are reasonably settled in a disk with weak turbulence, then the fractional abundance of gas-phase CO in the warm molecular layer can eventually be reduced by an order of magnitude as CO diffuses into the cold midplane and then freezes out. However, turbulence limits for the inner disk of TW Hya would have to be obtained to assess the feasibility of this mechanism.

Conversely, rather than interpreting the disk outside 15 au as being CO depleted in the warm molecular layer, the inner disk may be enhanced in CO if ice-coated particles drift inward and the ice subsequently sublimates (e.g., Cuzzi & Zahnle 2004; Stammer et al. 2017). The models investigating this effect have so far been one-dimensional. Further study on the heights at which this abundance enhancement occurs would help determine the impact on CO emission, since enhancement limited to the midplane would not make much difference to optically thick emission.

While gas density substructures and CO depletion have heretofore been discussed as separate possibilities, it is worth considering the extent to which they may be coupled. Reduced gas and dust surface densities lead to reduced UV opacities, which may allow UV radiation to dissociate CO more easily within the disk gaps (e.g., Visser et al. 2009). In addition, bumps and dips in the gas surface density profile can regulate dust transport and growth (e.g., Whipple 1972; Pinilla et al. 2012b), which in turn may affect the efficiency of the

grain surface reactions that serve as carbon sinks. Further chemical modeling would be useful to examine the extent to which CO depletion can be mediated by gas and dust gaps.

5.2. Possible Origins of the Radial Spectral Index Variations

We discuss below potential explanations for the appearance of the TW Hya continuum spectral index map, which shows a striking pattern of low values at the bright emission rings and high values within the emission gaps.

5.2.1. Radial Variation in Grain Sizes

Radial variations in α are often attributed to spatially varying grain size distributions in protoplanetary disks (e.g., Pérez et al. 2012; Menu et al. 2014; Tsukagoshi et al. 2016). Previous multifrequency measurements of TW Hya have indicated the presence of centimeter-sized grains inward of $r \sim 15$ au and the exclusion of such large grains from the 25 au continuum gap (Wilner et al. 2005; Menu et al. 2014; Tsukagoshi et al. 2016). With the high angular resolution 290 GHz spectral index map, we can also improve constraints on the grain size distribution in the narrow gaps and bright rings outside 25 au.

Following Tsukagoshi et al. (2016), we estimate the intensity of the submillimeter dust emission as

$$I_\nu(r) = B_\nu(T_d(r))(1 - \exp[-\tau_\nu(r)]), \quad (21)$$

where B_ν is the Planck function, $T_d(r)$ is the dust temperature (assuming that the millimeter dust disk is essentially isothermal vertically), and $\tau_\nu(r) = \tau_{290 \text{ GHz}}(r)(\nu/290 \text{ GHz})^\beta$ is the dust optical depth. The spectral index is then

$$\alpha(r) = 3 - x \frac{\exp x}{\exp x - 1} + \beta(r) \frac{\tau_\nu(r)}{\exp \tau_\nu(r) - 1}, \quad (22)$$

where $x = \frac{h\nu}{k_B T_d(r)}$.

The three unknowns are β , T_d , and τ_ν . While there are not sufficient constraints to solve for all three unknowns, useful limits can be placed on β . Figure 9 shows dust temperatures as a function of brightness temperatures for different fixed values of τ , and then α as a function of τ and β for a fixed brightness temperature of 11 K. The value of 11 K is chosen based on the brightness temperatures of the 290 GHz continuum emission rings at 35 and 45 au. Because β decreases as the maximum grain size increases, the upper limit on β should be the ISM value of ≈ 1.7 (Draine 2006), when no grain growth has occurred. Since α decreases when τ increases and when β decreases, placing a lower limit on τ also places a lower limit on β when α is known.

The dust temperature is likely no more than 30 K in the gaps and rings beyond a radius of 25 au in the TW Hya, given that CO freezeout is expected to commence in the midplane somewhere between 11 and 33 au (e.g., Qi et al. 2013; Nomura et al. 2016; Zhang et al. 2017). The brightness temperatures at radii from 25 to 50 au range from 10 to 12 K. Using Equation (21), this suggests that $\tau \gtrsim 0.25$ at 290 GHz in the gaps and rings outside 25 au.

The peak α values at the 25, 41, and 47 au continuum emission gaps are between 2.6 and 2.7. A lower bound of $\tau = 0.25$ indicates that $\beta \gtrsim 1$ in order to reproduce these α values, which would allow for grain growth up to a few millimeters (Draine 2006). In contrast, the low α values measured at the bright emission rings at 35 and 45 au are

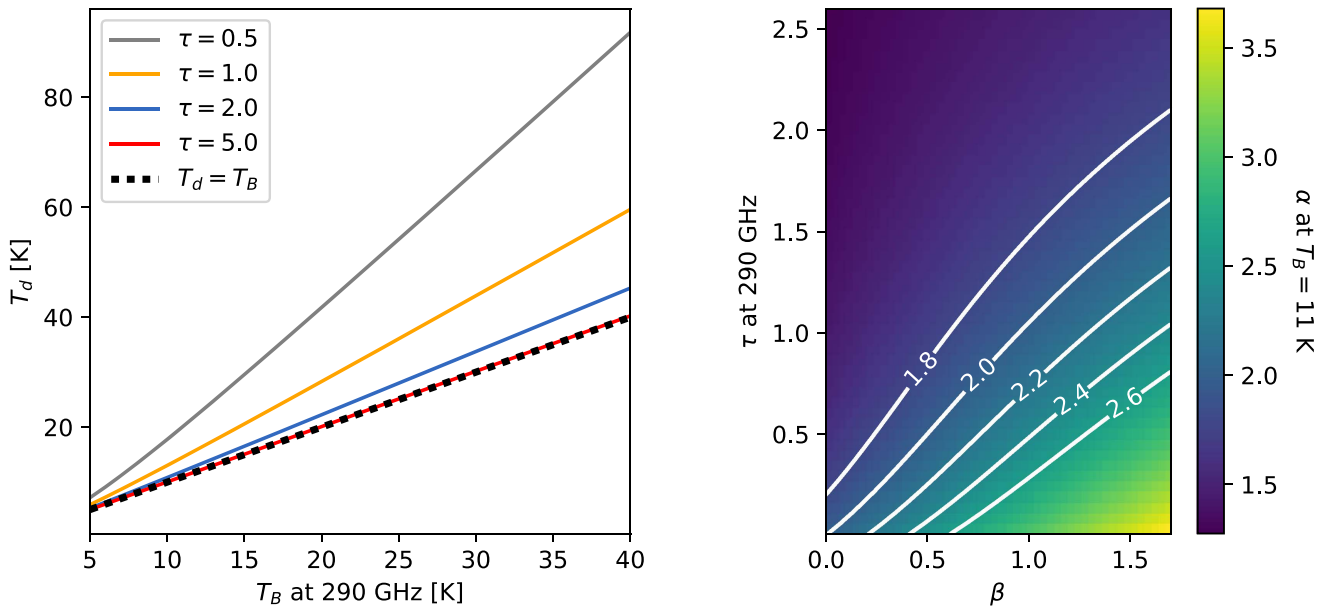


Figure 9. Left: plot of the relationship between T_B and T_d , computed at $\nu = 290$ GHz and for several values of τ . Right: plot of α at $T_B = 11$ K as a function of τ and β .

compatible with $\beta \gtrsim 0.4$, which allows for centimeter-sized grains (e.g., Pérez et al. 2012).

Tsukagoshi et al. (2016) interpreted the high spectral index value in the 25 au continuum gap as a signature of an embedded planet creating a pressure gradient that allows small grains to enter the gap but excludes large grains. This mechanism, known as dust filtration, is modeled in detail by Rice et al. (2006), Paardekooper & Mellema (2006), Zhu et al. (2012), and Pinilla et al. (2012a), among others. Dust filtration may also explain the gaps at 41 and 47 au, given their similar spectral index signatures.

5.2.2. Optical Depth Variations

While spatially varying grain size distributions can generate the observed spectral index profile, an alternative scenario worth considering is that the radial spectral index variations are largely tracing optical depth variations instead. Previous analyses of millimeter continuum emission concluded that $\tau \sim 1$ at $r < 15$ au in the TW Hya disk, in part based on the low spectral index values measured in the inner disk (Andrews et al. 2016; Tsukagoshi et al. 2016; Zhang et al. 2017). However, the high-resolution 290 GHz spectral index radial profile also reveals low spectral index values of $\alpha \approx 2$ at the locations of the bright emission rings at $r \approx 35$ au and $r \approx 45$ au, raising the question whether these are also marginally optically thick. We note that given the systematic uncertainties discussed in Section 3, it is possible that the true α profile is shifted upward by up to $\Delta\alpha = 0.4$, which would imply that nearly the whole millimeter dust disk is optically thin. For the sake of simply formulating a plausibility argument for the optically thick scenario, though, the remainder of the calculations in this section will take the spectral index profile in Figure 1 at face value.

Referring again to Figure 9, two points are worth emphasizing. First, low brightness temperatures are sometimes taken as prima facie evidence that the dust is optically thin, since the brightness temperature and dust temperature should be equal at large optical depths. The first panel of Figure 9 illustrates,

though, that even at an optical depth as high as $\tau = 1$, the brightness temperature is $\sim 30\%$ lower than the corresponding dust temperature. Thus, while Zhang et al. (2017) point out that adopting the brightness temperature as the midplane dust temperature would yield an unrealistically cold disk, a value of $\tau = 1$ corresponds to midplane temperatures that are only a few degrees lower than previous TW Hya models (e.g., Qi et al. 2013; Zhang et al. 2017). Second, $\alpha = 2$ is sometimes quoted as the lower bound set by optically thick emission, but this is specific to the Rayleigh–Jeans limit. The second panel of Figure 9 illustrates that at millimeter wavelengths, emission can still be optically thin when $\alpha = 2$, provided that β is small (and therefore grain sizes are large). For a dust temperature of 11 K, which can occur in the outer regions of protoplanetary disks, α can be as low as 1.2 in the optically thick limit at 290 GHz.

Figure 1 shows that the azimuthally averaged spectral index values range from roughly 2.1 to 2.3 inside the bright emission rings at 35 and 45 au. These α values are possible if $\tau \gtrsim 1.5$ (see Figure 9), still allowing the rings to be marginally optically thick. Even higher local values of τ may be compatible with the low brightness temperatures if the bright emission rings at 35 and 45 au are actually a series of unresolved rings that result in a low beam filling factor (e.g., Ricci et al. 2012). Andrews et al. (2016) tentatively identified additional emission gaps between 30 and 35 au, noting that higher angular resolution and sensitivity would be needed to confirm.

High dust optical depths imply high surface densities, so the gravitational stability of the potential unresolved narrow rings should be considered. The stability of the rings can be crudely estimated with Toomre’s Q parameter (Toomre 1964), where $Q = c_s \Omega / \pi G \Sigma$. (This estimate does require the assumption of a geometrically thin disk, which may not necessarily be true for TW Hya.) Assuming an ISM gas-to-dust ratio of 100, $\Sigma \approx 100 \Sigma_{\text{dust}} \approx 100 \tau_{\text{dust}} / \kappa_{\text{dust}}$. We adopt a dust opacity at 290 GHz of $\kappa = 3.3 \text{ cm}^2 \text{ g}^{-1}$, based on the Mie scattering calculations reported in Andrews et al. (2009) for spherical grains with a minimum radius of $a = 0.005 \mu\text{m}$, a maximum radius of 1 mm, a power-law distribution of $n(a) \propto a^{-3.5}$, silicate and graphite abundances derived in Mathis et al. (1977),

and dielectric functions from Draine & Lee (1984) and Weingartner & Draine (2001). For a stellar mass of $0.88 M_{\odot}$ and an isothermal sound speed calculated at a temperature of 15 K, $Q > 1$ for $\tau_{\text{dust}} < 3.2$ at 35 au and for $\tau_{\text{dust}} < 2.2$ at 45 au, suggesting that the rings can be optically thick and remain marginally gravitationally stable. Our calculation for Q scales with the ratio $\kappa_{\text{dust}}/\tau_{\text{dust}}$. Based on a distribution-of-hollow-spheres calculation for carbonaceous silicates, Woitke et al. (2016) advocate for the use of higher dust opacity values compared to the typically used Mie scattering values. Such higher opacity values would allow higher dust optical depths while maintaining gravitational stability. While optical depth effects may largely be sufficient to explain the spectral index at the gaps and rings between 25 and 45 au, the final rise in the spectral index near the 47 au emission gap is probably at least partially due to radial changes in β , since the peak in the spectral index profile is shifted slightly outward from the 47 au gap. The continuum intensity depends on temperature and optical depth, so if the radial temperature gradient is not too steep, the radial locations of the minima in the emission profiles would be close to the locations of the minima in the optical depth profiles. On the other hand, α has an additional dependence on β . The 47 au emission gap is not far from the edge of the millimeter dust disk, so the nearby rise in the spectral index may be influenced both by the deficit of material within the gap itself and by the bulk loss of large dust grains in the outer disk.

5.2.3. Comparison to Other Sources

Our calculations raise the possibility that all of the bright rings in the TW Hya millimeter continuum are marginally optically thick. This possibility has been suggested for other disks as well—to explain the correlation between the continuum luminosity and emitting area for a large disk sample, Tripathi et al. (2017) proposed that these disks consist of narrow, optically thick rings. Dust masses are often estimated using the Beckwith et al. (1990) formula assuming optically thin millimeter disk emission. If most disks are made up of optically thick rings, then dust masses have been systematically underestimated. In this case, CO or gas depletion may be even more severe than currently estimated, although large line optical depths may also contribute to underestimates of the amounts of CO or gas (e.g., Ansdell et al. 2016; Barenfeld et al. 2016; Long et al. 2017). High-resolution, multiband ALMA surveys of protoplanetary disks can determine whether other disks have continuum emission and spectral index profiles similar to those of TW Hya.

Only one other protoplanetary disk, that of HL Tau, has had its millimeter spectral index mapped at an angular resolution comparable to the TW Hya observations (ALMA Partnership et al. 2015). The features are strikingly similar to those of TW Hya—the bright dust emission rings correspond to low spectral index values of $\alpha \approx 2$ and the emission gaps correspond to high values of $\alpha \approx 3$. HL Tau and TW Hya may therefore reflect a common pattern in disks. If this is the case, the abrupt changes in the radial spectral index profiles may correspond to characteristic width scales for disk gaps. Measuring gap widths from intensity profiles is associated with significant ambiguity because an underlying “unperturbed” profile has to be assumed (e.g., Akiyama et al. 2016; Kanagawa et al. 2016). Hydrodynamic models of planet-forming disks often predict gap widths as a function of planet mass (e.g., Fouchet et al. 2010; Duffell & MacFadyen 2013; Zhu et al. 2013; Dong et al. 2015;

Jin et al. 2016), so linking gap widths in physical models to the widths of rings in resolved spectral index profiles may be useful for placing upper limits on the masses of potential embedded planets. However, it is currently ambiguous which, if any, features in the TW Hya disk are associated with embedded planets. While recent hydrodynamic simulations suggest that a single low-mass planet can create multiple gaps reminiscent of those observed in the millimeter continuum emission of TW Hya (Bae et al. 2017; Dong & Fung 2017), van Boekel et al. (2017) note that their derived gas surface density profile differs from predictions of gaps opened by planets in Duffell (2015).

5.3. Improving Constraints on the Structure of the TW Hya Disk

While relatively simple parameterizations of the molecular abundance and temperature structures can reasonably reproduce the radial features observed in the single ^{12}CO transition available at high resolution, better constraints need to be obtained on the vertical structure. Observing multiple transitions of all the isotopologues at comparably high angular resolution can reduce uncertainties with respect to the vertical distribution of CO. For example, whereas the inner edge of our ^{12}CO surface density gap lies at a radius of 15 au, Zhang et al. (2017) constrained the inner edge of the gap to lie at a radius of 22 au for C^{18}O . This modest difference may be due to the coarser angular resolution of the C^{18}O observations, but alternatively it could result from the onset radius of CO or gas depletion varying slightly with height, or from isotope-selective effects. Higher-resolution observations of C^{18}O would clarify the nature of this apparent difference. Several works have also suggested that the inner few au of the TW Hya disk may either be warped or feature deviations from Keplerian rotation (e.g., Roberge et al. 2005; Rosenfeld et al. 2012; Debes et al. 2017). These effects alone cannot create the axisymmetric substructures observed in the main CO isotopologues, but they would be worth considering in a more detailed analysis of the disk vertical structure.

With the observations currently available, it is not straightforward to distinguish between gas disk substructure and CO depletion as the main explanation for the CO emission morphology. Although the gas surface density profile derived by van Boekel et al. (2017) appears to disfavor the possibility that CO is closely tracing the gas distribution, they assumed a constant gas-to-small-dust ratio. TW Hya is one of the few sources for which a disk gas mass has been measured without having to assume either an X_{CO} value or a gas-to-dust ratio, thanks to *Herschel* observations of HD (Bergin et al. 2013). Although Cleaves et al. (2015) find that the bulk gas-to-dust ratio of the TW Hya disk is consistent with that of the ISM, the spatially unresolved HD observations do not exclude localized gas depletions.

The question of how to reliably distinguish CO and gas depletion in disks has been raised in a number of works aiming to estimate the gas masses of protoplanetary disks from millimeter/submillimeter surveys of CO and dust (e.g., Barenfeld et al. 2016; Long et al. 2017; Miotello et al. 2017). As the nearest disk, TW Hya may be the most important test case for breaking the degeneracy. Miotello et al. (2017) suggest measuring hydrocarbon abundances to check for evidence of CO depletion, since hydrocarbons are believed to be a carbon sink when CO is destroyed by He^+ . C_2H and $c\text{-C}_3\text{H}_2$ have been observed in the

TW Hya disk at $\approx 0''.4$ resolution by Bergin et al. (2016); re-observing at higher resolution to compare to CO emission, accompanied by chemical modeling, may yield additional insight into whether and how X_{CO} varies throughout the disk.

(Magneto)hydrodynamic simulations tailored to TW Hya would also shed some light on whether the CO emission morphology is tracing gas substructure rather than chemical depletion. While a direct correspondence between the CO and millimeter dust structures is not obvious in the data presented in this work, disk models indicate that embedded planets and dead zones can create gaps and rings in gas and millimeter dust that are offset from one another and differ in depth and width (e.g., Pinilla et al. 2016; Ruge et al. 2016; Dong et al. 2017; Facchini et al. 2017b). A model that simultaneously matches the TW Hya millimeter observations and yields a gas surface density profile similar to that of the inferred CO surface density profile would be compelling evidence for gas substructure.

6. Summary

We presented new ALMA observations of $^{12}\text{CO } J = 3 - 2$ in the TW Hya disk at a spatial resolution of 8 au, representing one of the highest-resolution images so far of molecular line emission in a protoplanetary disk. We also reprocessed archival 1.3 mm and 870 μm continuum data to produce a spectral index map at a spatial resolution of 2 au. Our results and conclusions are as follows:

1. The ^{12}CO images exhibit radial emission breaks coinciding with gaps and rings previously observed in ^{13}CO and C^{18}O emission. We employ LTE radiative transfer modeling to demonstrate that the ^{12}CO emission morphology can be reasonably reproduced by a sharp drop in the CO column density at $r = 15$ au and a secondary peak at 70 au.
2. Analysis of the ^{12}CO brightness temperatures and radiative transfer modeling suggest that the inferred CO column density variations are likely not associated with the onset of freezeout in the midplane. We propose instead that the variations in the ^{12}CO column density arise either from spatial variations in X_{CO} or from gas density reductions in the warm molecular layer of the disk. Based on similar features observed in the much lower abundance isotopologues, we further argue that these variations are likely present throughout most of the vertical extent of the warm layer. Distinguishing between CO depletion and gas disk substructures would be facilitated by obtaining more stringent constraints on the temperature structure of the disk and observing complementary molecular tracers of carbon depletion.
3. The 290 GHz spectral index map shows a striking contrast between spectral index values of ~ 2 at the bright continuum emission rings and ~ 2.7 at the emission gaps. The high spectral index values within the emission gaps suggest that the maximum grain size is limited to a few millimeters. The low spectral index values at the continuum emission rings may be a signature of grain growth to centimeter sizes, but a plausible alternative explanation is that the rings are all marginally optically thick. The latter possibility is worth investigating for a

larger sample of disks to determine whether disk dust masses are being systematically underestimated.

We thank the NAASC staff for their advice on data reduction; Roy van Boekel, Hannah Jang-Condell, and Ke Zhang for their discussions of TW Hya; and the referee for useful comments. This paper makes use of ALMA data [ADS/JAO.ALMA#2012.1.00422.S](#), [ADS/JAO.ALMA#2013.1.00114.S](#), [ADS/JAO.ALMA#2013.1.00196.S](#), [ADS/JAO.ALMA#2013.1.00198.S](#), [ADS/JAO.ALMA#2013.1.00387.S](#), [ADS/JAO.ALMA#2013.1.01397.S](#), [ADS/JAO.ALMA#2015.1.00686.S](#), [ADS/JAO.ALMA#2015.A.00005.S](#), and [ADS/JAO.ALMA#2016.1.00629.S](#). ALMA is a partnership of ESO (representing its member states), NSF (USA), and NINS (Japan), together with NRC (Canada) and NSC and ASIAA (Taiwan), in cooperation with the Republic of Chile. The Joint ALMA Observatory is operated by ESO, AUI/NRAO, and NAOJ. The National Radio Astronomy Observatory is a facility of the National Science Foundation operated under cooperative agreement by Associated Universities, Inc. J.H. acknowledges support from the National Science Foundation Graduate Research Fellowship under grant No. DGE-1144152 and from NRAO Student Observing Support. L.I.C. acknowledges the support of NASA through Hubble Fellowship grant *HST*-HF2-51356.001-A awarded by the Space Telescope Science Institute, which is operated by the Association of Universities for Research in Astronomy, Inc., for NASA, under contract NAS 5-26555. K.I.Ö. acknowledges funding through a Packard Fellowship for Science and Engineering from the David and Lucile Packard Foundation. T.B. acknowledges funding from the European Research Council (ERC) under the European Union’s Horizon 2020 research and innovation program under grant agreement No. 714769.

Software: CASA (McMullin et al. 2007), *AstroPy* (Astropy Collaboration et al. 2013), *analysisUtils* (https://casaguides.nrao.edu/index.php/Analysis_Uilities), *RADMC-3D* (Dullemond 2012), *radmc3dPy* (<http://www.ast.cam.ac.uk/~juhasz/radmc3dPyDoc/index.html>), *vis_sample* (Czekala et al. 2015; Loomis et al. 2017).

Facility: ALMA.

Appendix A Additional Calibrator Details

Table 3 of Appendix A lists the bandpass, phase, and flux calibrators used for all the data presented in this work, as well as the reference frequency, flux density, and spectral index used to model the spectra of the quasars that served as flux calibrators. The ALMA calibrator catalog flux density values that served as the basis for the flux calibration on 2016 December 30 for program 2016.1.00629.S were revised downward by 8% after delivery of the original data (T. Hunter, private communication), so we rescaled the fluxes of the data sets accordingly. In all other cases, we retained the original flux calibration specified in the ALMA archive.

Table 3
Calibrator Sources and Calibration Models

Program	Date(s)	Bandpass Calibrator	Phase Calibrator	Flux Calibrator	Reference Frequency (GHz)	Flux Density (Jy)	Spectral Index
2012.1.00422.S	2015 May 14	J1256–057	J1037–2934	Titan ^a
2013.1.00114.S	2014 Jul 19	J1037–2934	J1037–2934	Pallas ^a
2013.1.00196.S	2014 Dec 24	J1256–0547	J1037–2934	Callisto ^a
	2015 Apr 5	J1256–0547	J1037–2934	J1037–295	330.624	0.736	–0.53
2013.1.00198.S	2014 Dec 31	J1058+0133	J1037–2934	Ganymede ^a
	2015 Jun 15	J1058+0133	J1037–2934	Callisto ^a
2013.1.00387.S	2015 May 13	J1037–2934	J1037–2934	Ganymede ^a
2013.1.01397.S	2015 May 19–20	J1058+0133	J1037–2934	J1037–295	335.726	0.587	–0.534
2015.1.00686.S	2015 Nov 23	J1058+1033	J1103–3251	J1037–2934	350.638	0.604	–0.492
	2015 Nov 30	J1058+0133	J1103–3251	J1107–4449	350.640	0.542	–0.711
	2015 Dec 1	J1058+0133	J1103–3251	J1037–2934	350.640	0.627	–0.468
2015.A.00005.S	2015 Dec 1	J1107–4449	J1103–3251	J1037–2934	233.0	0.759	–0.468
2016.1.00629.S	2016 Dec 30	J1058+0133	J1037–2934	J1037–2934 ^b	345.810	0.728	–0.357
	2016 Dec 30	J1058+0133	J1037–2934	J1058+0133 ^b	345.809	3.568	–0.395
	2017 Jul 4	J1037–2934	J1037–2934	J1037–2934	345.755	0.788	–0.592
	2017 Jul 9	J1058+0133	J1037–2934	J1037–2934	345.756	0.788	–0.592
	2017 Jul 14	J1058+0133	J1037–2934	J1037–2934	345.756	0.646	–0.647
	2017 Jul 20	J1058+0133	J1037–2934	J1037–2934	345.758	0.646	–0.647
	2017 Jul 21	J1058+0133	J1037–2934	J1256–0547	345.757	7.4223	–0.495

Notes.

^a Using the Butler-JPL-Horizons 2012 models.

^b Flux density values adjusted from original delivered scripts to correspond with updated calibrator catalog values. All other values are retained from the ALMA archival scripts.

Appendix B Band 6 and 7 Continuum Images and Profiles

The 1.3 mm and 870 μm continuum images and radial brightness temperature profiles are shown in Figure 10. The inclusion of additional archival data provides a modest

improvement in image fidelity over the images from Andrews et al. (2016) and Tsukagoshi et al. (2016). The Planck equation is used to compute brightness temperature because the Rayleigh–Jeans approximation is typically poor for submillimeter observations of protoplanetary disks.

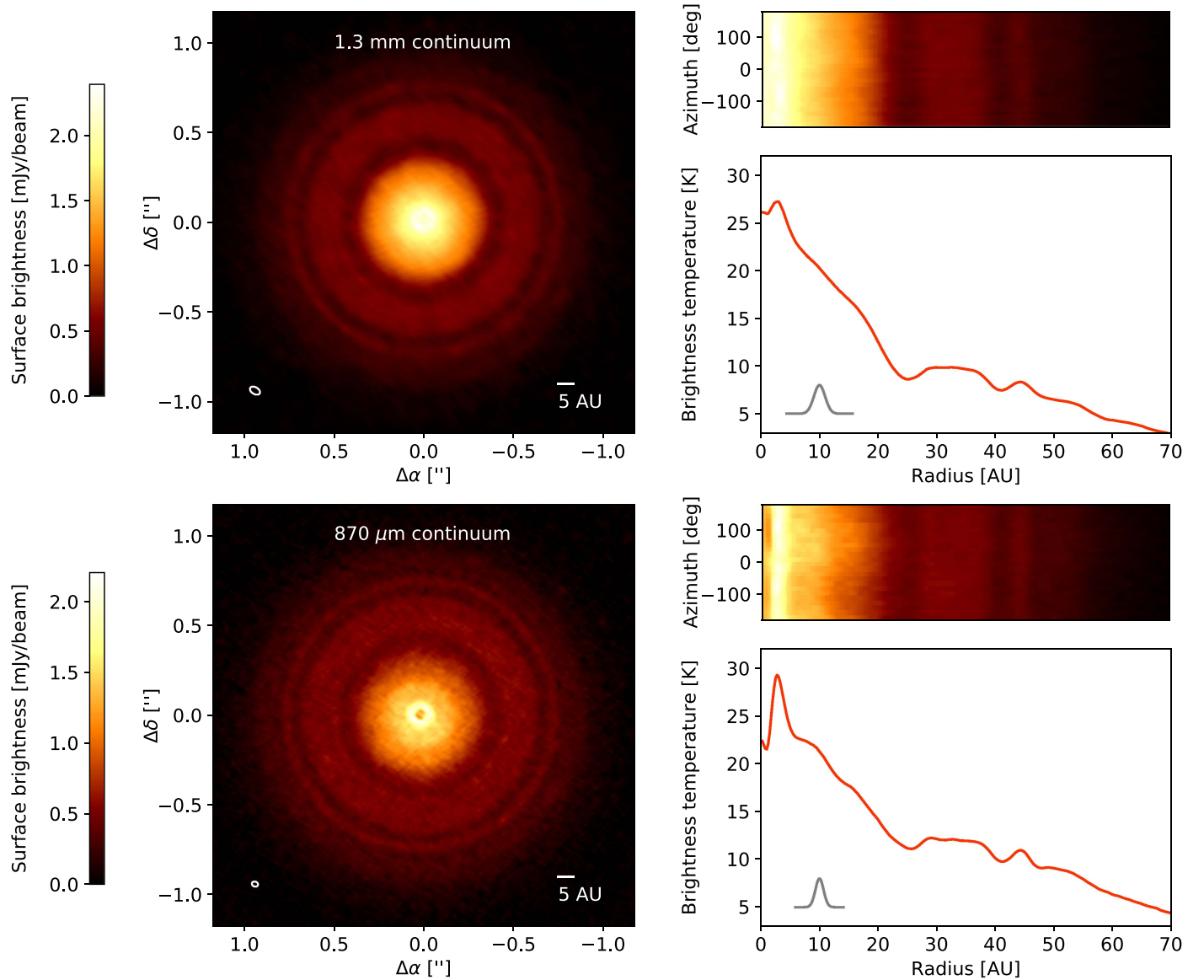


Figure 10. Top left: image of 1.3 mm continuum emission. The synthesized beam, shown in the lower left corner, has FWHM dimensions of 61×38 mas (3.6×2.2 au) and a position angle of $59^\circ.4$. The rms is $18 \mu\text{Jy beam}^{-1}$. Top right: 1.3 mm continuum emission deprojected and replotted as a function of radius and azimuth, with the deprojected, azimuthally averaged radial brightness temperature profile shown underneath. The Gaussian profile shows the FWHM of the minor axis of the synthesized beam. Bottom left: image of $870 \mu\text{m}$ continuum emission. The synthesized beam has FWHM dimensions of 35×28 mas (2.1×1.7 au) and a position angle of $69^\circ.9$. The rms is $31 \mu\text{Jy beam}^{-1}$. Bottom right: $870 \mu\text{m}$ continuum emission plotted in polar coordinates, with the corresponding averaged radial brightness temperature profile underneath.

Appendix C

$^{13}\text{CO } J = 3 - 2$ Channel Maps

For comparison with the ^{12}CO data, we image $^{13}\text{CO } J = 3 - 2$ in the TW Hya disk by combining archival observations from programs 2012.1.00422.S, 2013.1.00196.S, and 2013.1.01397.S. Integrated intensity maps of ^{13}CO from 2012.1.00422.S and 2013.1.01397.S were presented separately in Schwarz et al. (2016) and Nomura et al. (2016), respectively. The raw data were downloaded from the ALMA archive and calibrated using the accompanying scripts. The observation setups are described in Table 1. The ^{13}CO data from each program were phase self-calibrated with solutions obtained

from the line-free channels within the same SPWs. The continuum was then subtracted from the line emission in the visibility plane using the `uvcontsub` task. For the sake of comparison with the ^{12}CO channel maps, the `mstransform` task was used to average and regrid the spectral line visibilities.

The data sets were imaged together with multiscale CLEAN, using scales of 0, 0.25, 0.5, 0.75, and 1.25 arcsec with Briggs weighting (robust = 0). The resulting image has a synthesized beam with an FWHM of $0''.44 \times 0''.35$ (26×21 au) at a position angle of $71^\circ.2$. The rms measured in nearby signal-free channels is $\approx 3.5 \text{ mJy beam}^{-1}$. As with the ^{12}CO data, a primary beam correction was applied to the image cube, shown in Figure 11 in Appendix C.

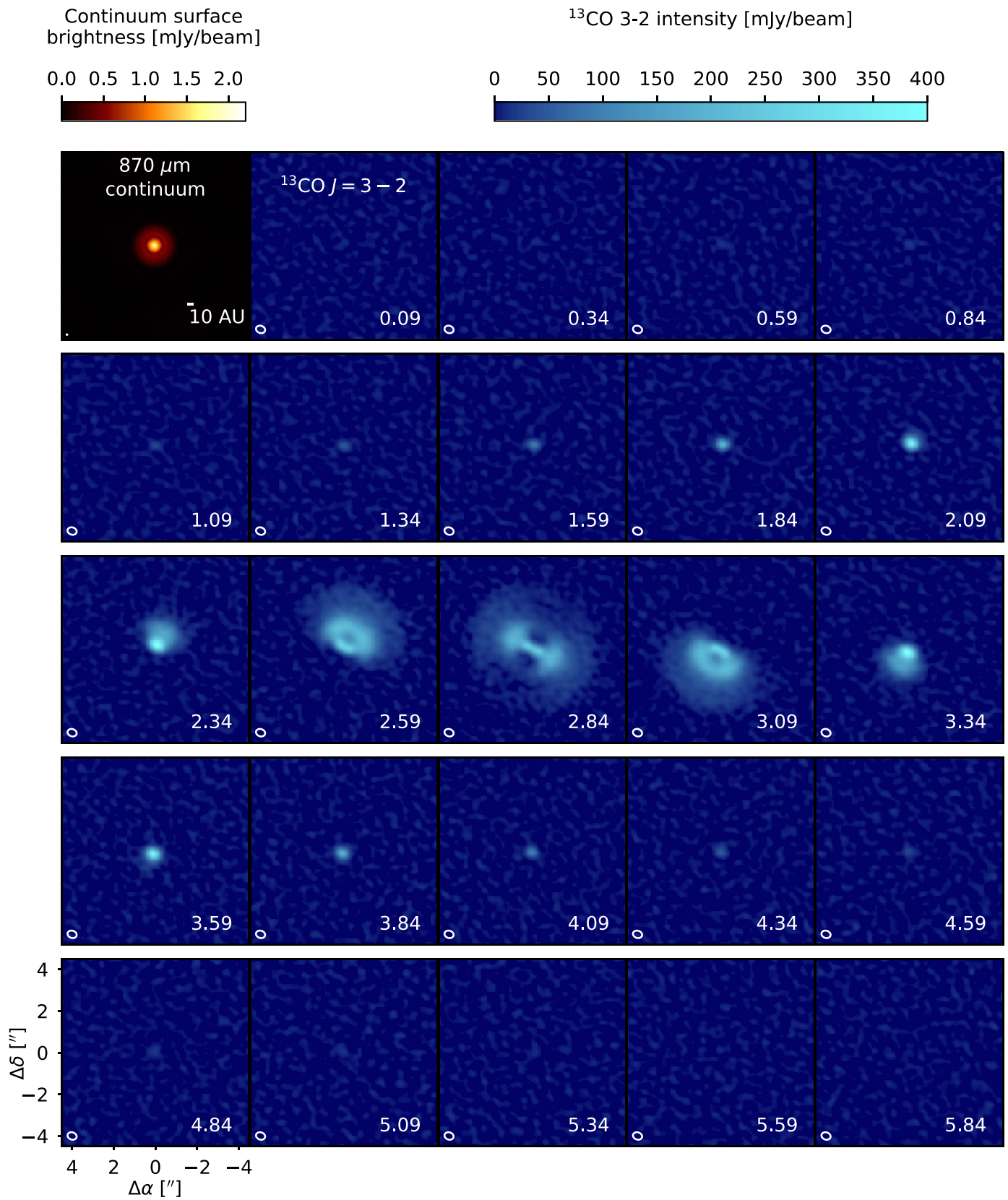












Figure 11. Channel maps of the $^{13}\text{CO } J = 3 - 2$ transition in the TW Hya disk, along with the $870 \mu\text{m}$ continuum emission in the upper leftmost panel shown on the same spatial scale. Synthesized beams are drawn in the lower left corner of each panel. The LSR velocity (km s^{-1}) for each ^{13}CO channel is shown in the lower right corner, matching the velocities shown for ^{12}CO in Figure 2.

ORCID iDs

Jane Huang  <https://orcid.org/0000-0001-6947-6072>
 Sean M. Andrews  <https://orcid.org/0000-0003-2253-2270>
 L. Ilseoree Cleeves  <https://orcid.org/0000-0003-2076-8001>
 Karin I. Öberg  <https://orcid.org/0000-0001-8798-1347>
 David J. Wilner  <https://orcid.org/0000-0003-1526-7587>
 Xuening Bai  <https://orcid.org/0000-0001-6906-9549>
 Til Birnstiel  <https://orcid.org/0000-0002-1899-8783>
 John Carpenter  <https://orcid.org/0000-0003-2251-0602>
 Andrea Isella  <https://orcid.org/0000-0001-8061-2207>
 Zhaohuan Zhu  <https://orcid.org/0000-0003-3616-6822>

References

- Aikawa, Y., & Herbst, E. 1999, *A&A*, **351**, 233
 Aikawa, Y., Umebayashi, T., Nakano, T., & Miyama, S. M. 1997, *ApJL*, **486**, L51
 Akiyama, E., Hasegawa, Y., Hayashi, M., & Iguchi, S. 2016, *ApJ*, **818**, 158
 Akiyama, E., Muto, T., Kusakabe, N., et al. 2015, *ApJL*, **802**, L17
 ALMA Partnership, Brogan, C. L., Pérez, L. M., et al. 2015, *ApJL*, **808**, L3
 Andrews, S. M., Wilner, D. J., Hughes, A. M., et al. 2012, *ApJ*, **744**, 162
 Andrews, S. M., Wilner, D. J., Hughes, A. M., Qi, C., & Dullemond, C. P. 2009, *ApJ*, **700**, 1502
 Andrews, S. M., Wilner, D. J., Zhu, Z., et al. 2016, *ApJL*, **820**, L40
 Ansdell, M., Williams, J. P., van der Marel, N., et al. 2016, *ApJ*, **828**, 46
 Astropy Collaboration, Robitaille, T. P., Tollerud, E. J., et al. 2013, *A&A*, **558**, A33
 Bae, J., Zhu, Z., & Hartmann, L. 2017, *ApJ*, **850**, 201
 Barenfeld, S. A., Carpenter, J. M., Ricci, L., & Isella, A. 2016, *ApJ*, **827**, 142
 Beckwith, S. V. W., Sargent, A. I., Chini, R. S., & Guesten, R. 1990, *AJ*, **99**, 924
 Bergin, E. A., Cleeves, L. I., Crockett, N., & Blake, G. A. 2014, *FaDi*, 168
 arXiv:1405.7394
 Bergin, E. A., Cleeves, L. I., Gorti, U., et al. 2013, *Natur*, **493**, 644
 Bergin, E. A., Du, F., Cleeves, L. I., et al. 2016, *ApJ*, **831**, 101
 Birnstiel, T., & Andrews, S. M. 2014, *ApJ*, **780**, 153
 Birnstiel, T., Andrews, S. M., Pinilla, P., & Kama, M. 2015, *ApJL*, **813**, L14
 Birnstiel, T., Ricci, L., Trotta, F., et al. 2010, *A&A*, **516**, L14
 Boehler, Y., Weaver, E., Isella, A., et al. 2017, *ApJ*, **840**, 60
 Bruderer, S., van Dishoeck, E. F., Doty, S. D., & Herczeg, G. J. 2012, *A&A*, **541**, A91
 Calvet, N., D'Alessio, P., Hartmann, L., et al. 2002, *ApJ*, **568**, 1008
 Christiaens, V., Casassus, S., Perez, S., van der Plas, G., & Ménard, F. 2014, *ApJL*, **785**, L12
 Cleeves, L. I. 2016, *ApJL*, **816**, L21
 Cleeves, L. I., Bergin, E. A., Qi, C., Adams, F. C., & Öberg, K. I. 2015, *ApJ*, **799**, 204
 Collings, M. P., Dever, J. W., Fraser, H. J., McCoustra, M. R. S., & Williams, D. A. 2003, *ApJ*, **583**, 1058
 Cornwell, T. J. 2008, *ISTSP*, **2**, 793
 Cridland, A. J., Pudritz, R. E., & Alessi, M. 2016, *MNRAS*, **461**, 3274
 Cuzzi, J. N., & Zahnle, K. J. 2004, *ApJ*, **614**, 490
 Czekala, I., Andrews, S. M., Jensen, E. L. N., et al. 2015, *ApJ*, **806**, 154
 Dartois, E., Dutrey, A., & Guilloteau, S. 2003, *A&A*, **399**, 773
 Debes, J. H., Jang-Condell, H., Weinberger, A. J., Roberge, A., & Schneider, G. 2013, *ApJ*, **771**, 45
 Debes, J. H., Poteet, C. A., Jang-Condell, H., et al. 2017, *ApJ*, **835**, 205
 Dong, R., & Fung, J. 2017, *ApJ*, **835**, 146
 Dong, R., Li, S., Chiang, E., & Li, H. 2017, *ApJ*, **843**, 127
 Dong, R., Zhu, Z., & Whitney, B. 2015, *ApJ*, **809**, 93
 Draine, B. T. 2006, *ApJ*, **636**, 1114
 Draine, B. T., & Lee, H. M. 1984, *ApJ*, **285**, 89
 Duffell, P. C. 2015, *ApJL*, **807**, L11
 Duffell, P. C., & MacFadyen, A. I. 2013, *ApJ*, **769**, 41
 Dullemond, C. P. 2012, RADMC-3D: A Multi-purpose Radiative Transfer Tool, Astrophysics Source Code Library, ascl:1202.015
 Eisner, J. A., Chiang, E. I., & Hillenbrand, L. A. 2006, *ApJL*, **637**, L133
 Eistrup, C., Walsh, C., & van Dishoeck, E. F. 2016, *A&A*, **595**, A83
 Ercolano, B., Rosotti, G. P., Picogna, G., & Testi, L. 2017, *MNRAS*, **464**, L95
 Facchini, S., Birnstiel, T., Bruderer, S., & van Dishoeck, E. F. 2017a, *A&A*, **605**, A16
 Facchini, S., Pinilla, P., van Dishoeck, E. F., & de Juan Ovelar, M. 2017b, arXiv:1710.04418
 Favre, C., Cleeves, L. I., Bergin, E. A., Qi, C., & Blake, G. A. 2013, *ApJL*, **776**, L38
 Fayolle, E. C., Balfe, J., Loomis, R., et al. 2016, *ApJL*, **816**, L28
 Flaherty, K. M., Hughes, A. M., Rosenfeld, K. A., et al. 2015, *ApJ*, **813**, 99
 Flock, M., Ruge, J. P., Dzyurkevich, N., et al. 2015, *A&A*, **574**, A68
 Fouchet, L., Gonzalez, J.-F., & Maddison, S. T. 2010, *A&A*, **518**, A16
 Gaia Collaboration, Brown, A. G. A., Vallenari, A., et al. 2016, *A&A*, **595**, A2
 Guilloteau, S., Dutrey, A., Piétu, V., & Boehler, Y. 2011, *A&A*, **529**, A105
 Guilloteau, S., Piétu, V., Dutrey, A., & Guélin, M. 2006, *A&A*, **448**, L5
 Herbst, E., & Klemperer, W. 1973, *ApJ*, **185**, 505
 Hughes, A. M., Wilner, D. J., Andrews, S. M., Qi, C., & Hogerheijde, M. R. 2011, *ApJ*, **727**, 85
 Isella, A., Guidi, G., Testi, L., et al. 2016, *PhRvL*, **117**, 251101
 Jang-Condell, H., & Turner, N. J. 2012, *ApJ*, **749**, 153
 Jang-Condell, H., & Turner, N. J. 2013, *ApJ*, **772**, 34
 Jin, S., Li, S., Isella, A., Li, H., & Ji, J. 2016, *ApJ*, **818**, 76
 Kama, M., Bruderer, S., van Dishoeck, E. F., et al. 2016, *A&A*, **592**, A83
 Kamp, I., Thi, W.-F., Woitke, P., et al. 2017, *A&A*, **607**, A41
 Kanagawa, K. D., Muto, T., Tanaka, H., et al. 2016, *PASJ*, **68**, 43
 Kastner, J. H., Zuckerman, B., Weintraub, D. A., & Forveille, T. 1997, *Sci*, **277**, 67
 Long, F., Herczeg, G. J., Pascucci, I., et al. 2017, *ApJ*, **844**, 99
 Loomis, R. A., Öberg, K. I., Andrews, S. M., et al. 2017, *AJ*, submitted
 Lynden-Bell, D., & Pringle, J. E. 1974, *MNRAS*, **168**, 603
 Mathis, J. S., Rumpl, W., & Nordsieck, K. H. 1977, *ApJ*, **217**, 425
 McMullin, J. P., Waters, B., Schiebel, D., Young, W., & Golap, K. 2007, in ASP Conf. Ser. 376, *Astronomical Data Analysis Software and Systems XVI*, ed. R. A. Shaw, F. Hill, & D. J. Bell (San Francisco, CA: ASP), **127**
 Menu, J., van Boekel, R., Henning, T., et al. 2014, *A&A*, **564**, A93
 Miotello, A., Bruderer, S., & van Dishoeck, E. F. 2014, *A&A*, **572**, A96
 Miotello, A., van Dishoeck, E. F., Williams, J. P., et al. 2017, *A&A*, **599**, A113
 Nomura, H., Tsukagoshi, T., Kawabe, R., et al. 2016, *ApJL*, **819**, L7
 Öberg, K. I., & Bergin, E. A. 2016, *ApJL*, **831**, L19
 Öberg, K. I., Guzmán, V. V., Merchant, C. J., et al. 2017, *ApJ*, **839**, 43
 Öberg, K. I., Murray-Clay, R., & Bergin, E. A. 2011, *ApJL*, **743**, L16
 Paardekooper, S.-J., & Mellema, G. 2006, *A&A*, **453**, 1129
 Pavlyuchenkov, Y., Semenov, D., Henning, T., et al. 2007, *ApJ*, **669**, 1262
 Pérez, L. M., Carpenter, J. M., Chandler, C. J., et al. 2012, *ApJL*, **760**, L17
 Pinilla, P., Benisty, M., & Birnstiel, T. 2012a, *A&A*, **545**, A81
 Pinilla, P., Birnstiel, T., Ricci, L., et al. 2012b, *A&A*, **538**, A114
 Pinilla, P., Flock, M., Ovelar, M. d. J., & Birnstiel, T. 2016, *A&A*, **596**, A81
 Powell, D., Murray-Clay, R., & Schlichting, H. E. 2017, *ApJ*, **840**, 93
 Qi, C., Ho, P. T. P., Wilner, D. J., et al. 2004, *ApJL*, **616**, L11
 Qi, C., Öberg, K. I., Wilner, D. J., et al. 2013, *Sci*, **341**, 630
 Qi, C., Wilner, D. J., Aikawa, Y., Blake, G. A., & Hogerheijde, M. R. 2008, *ApJ*, **681**, 1396
 Rapson, V. A., Kastner, J. H., Millar-Blanchaer, M. A., & Dong, R. 2015, *ApJL*, **815**, L26
 Rau, U., & Cornwell, T. J. 2011, *A&A*, **532**, A71
 Reboussin, L., Wakelam, V., Guilloteau, S., Hersant, F., & Dutrey, A. 2015, *A&A*, **579**, A82
 Ricci, L., Testi, L., Natta, A., et al. 2010, *A&A*, **512**, A15
 Ricci, L., Trotta, F., Testi, L., et al. 2012, *A&A*, **540**, A6
 Rice, W. K. M., Armitage, P. J., Wood, K., & Lodato, G. 2006, *MNRAS*, **373**, 1619
 Roberge, A., Weinberger, A. J., & Malumuth, E. M. 2005, *ApJ*, **622**, 1171
 Rosenfeld, K. A., Andrews, S. M., Hughes, A. M., Wilner, D. J., & Qi, C. 2013, *ApJ*, **774**, 16
 Rosenfeld, K. A., Qi, C., Andrews, S. M., et al. 2012, *ApJ*, **757**, 129
 Ruge, J. P., Flock, M., Wolf, S., et al. 2016, *A&A*, **590**, A17
 Sandford, S. A., & Allamandola, L. J. 1988, *Icar*, **76**, 201
 Schöier, F. L., van der Tak, F. F. S., van Dishoeck, E. F., & Black, J. H. 2005, *A&A*, **432**, 369
 Schwarz, K. R., Bergin, E. A., Cleeves, L. I., et al. 2016, *ApJ*, **823**, 91
 Simon, J. B., Hughes, A. M., Flaherty, K. M., Bai, X.-N., & Armitage, P. J. 2015, *ApJ*, **808**, 180
 Stammer, S. M., Birnstiel, T., Panić, O., Dullemond, C. P., & Dominik, C. 2017, *A&A*, **600**, A140
 Teague, R., Guilloteau, S., Semenov, D., et al. 2016, *A&A*, **592**, A49
 Teague, R., Semenov, D., Gorti, U., et al. 2017, *ApJ*, **835**, 228
 Toomre, A. 1964, *ApJ*, **139**, 1217
 Torres, C. A. O., Quast, G. R., da Silva, L., et al. 2006, *A&A*, **460**, 695
 Tripathi, A., Andrews, S. M., Birnstiel, T., & Wilner, D. J. 2017, *ApJ*, **845**, 44

- Tsukagoshi, T., Nomura, H., Muto, T., et al. 2016, [ApJL](#), **829**, L35
- van Boekel, R., Henning, T., Menu, J., et al. 2017, [ApJ](#), **837**, 132
- van der Marel, N., van Dishoeck, E. F., Bruderer, S., et al. 2016, [A&A](#), **585**, A58
- van der Marel, N., van Dishoeck, E. F., Bruderer, S., Pérez, L., & Isella, A. 2015, [A&A](#), **579**, A106
- van Dishoeck, E. F., Thi, W.-F., & van Zadelhoff, G.-J. 2003, [A&A](#), **400**, L1
- van't Hoff, M. L. R., Walsh, C., Kama, M., Facchini, S., & van Dishoeck, E. F. 2017, [A&A](#), **599**, A101
- Vasyunin, A. I., Semenov, D., Henning, T., et al. 2008, [ApJ](#), **672**, 629
- Visser, R., van Dishoeck, E. F., & Black, J. H. 2009, [A&A](#), **503**, 323
- Walsh, C., Loomis, R. A., Öberg, K. I., et al. 2016, [ApJL](#), **823**, L10
- Webb, R. A., Zuckerman, B., Platais, I., et al. 1999, [ApJL](#), **512**, L63
- Weinberger, A. J., Anglada-Escudé, G., & Boss, A. P. 2013, [ApJ](#), **762**, 118
- Weingartner, J. C., & Draine, B. T. 2001, [ApJ](#), **548**, 296
- Whipple, F. L. 1972, in *From Plasma to Planet*, ed. A. Elvius (New York: Wiley), 211
- Williams, J. P., & Best, W. M. J. 2014, [ApJ](#), **788**, 59
- Wilner, D. J., D'Alessio, P., Calvet, N., Claussen, M. J., & Hartmann, L. 2005, [ApJL](#), **626**, L109
- Wilson, T. L. 1999, [RPPh](#), **62**, 143
- Woitke, P., Kamp, I., & Thi, W.-F. 2009, [A&A](#), **501**, 383
- Woitke, P., Min, M., Pinte, C., et al. 2016, [A&A](#), **586**, A103
- Xu, R., Bai, X.-N., & Öberg, K. 2017, [ApJ](#), **835**, 162
- Yu, M., Willacy, K., Dodson-Robinson, S. E., Turner, N. J., & Evans, N. J., II 2016, [ApJ](#), **822**, 53
- Zhang, K., Bergin, E. A., Blake, G. A., et al. 2016, [ApJL](#), **818**, L16
- Zhang, K., Bergin, E. A., Blake, G. A., Cleaves, L. I., & Schwarz, K. R. 2017, [NatAs](#), **1**, 0130
- Zhang, K., Blake, G. A., & Bergin, E. A. 2015, [ApJL](#), **806**, L7
- Zhu, Z., Nelson, R. P., Dong, R., Espaillat, C., & Hartmann, L. 2012, [ApJ](#), **755**, 6
- Zhu, Z., Stone, J. M., & Rafikov, R. R. 2013, [ApJ](#), **768**, 143
- Zhu, Z., Stone, J. M., Rafikov, R. R., & Bai, X.-n 2014, [ApJ](#), **785**, 122